LBL-7204
c.2

SMALL-AMPLITUDE PERIODIC SLOSHING MODES OF A LIQUID IN A VERTICAL RIGHT CIRCULAR CYLINDER WITH A CONCAVE SPHEROIDAL BOTTOM

N. Albright and P. Concus

November 1977

Prepared for the U. S. Department of Energy
under Contract W-7405-ENG-48
and by the National Aeronautics and Space
Administration under Grant No. 67705-C

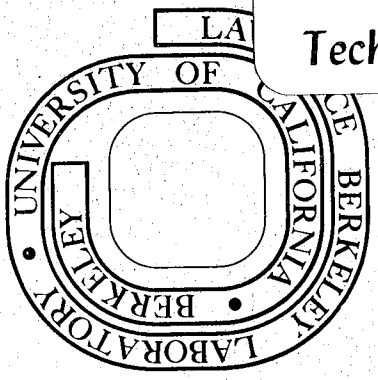

LBL-7204
c.2

LBL-7204

SMALL-AMPLITUDE PERIODIC SLOSHING MODES OF A LIQUID IN A VERTICAL RIGHT CIRCULAR CYLINDER WITH A CONCAVE SPHEROIDAL BOTTOM

by

N. ALBRIGHT & P. CONCUS

Lawrence Berkeley Laboratory
University of California
Berkeley, CA 94720

November, 1977

CONTENTS

ABSTRACT

In this paper we calculate the small-amplitude periodic sloshing modes of a liquid in a vertical right circular cylinder with a concave spheroidal bottom, for the case in which there is not sufficient liquid to cover the bottom entirely. Equilibrium free surfaces of the liquid were calculated by the program CAPIL for the case in which the ratio of the minor and major semi-axes of the spheroidal bottom was 0.724. Perturbations about these surfaces were calculated by the program SLOSH. For the fill heights that were studied, and to the accuracy of these calculations, we found the same critical Bond number, B_{crit}, for instability of the free surface as was found in the static analysis of P. Concus and I. Karasalo for the same test problem. Furthermore, in agreement with their calculation we also found no equilibrium surfaces for this problem for fill heights greater than 0.503 and for Bond numbers $B < B_{crit} < 0$. For fill heights ranging from 0.20 to 0.45 we found unstable equilibrium surfaces for a range of Bond numbers, $B_{conv} \leqslant B < B_{crit}$. Frequencies or growth rates were calculated for numerous equilibrium surfaces. Growth rates of the maximally unstable modes were calculated for fill height 0.30 and various Bond numbers.

1. Introduction

In this paper we calculate the small-amplitude, periodic sloshing modes of a liquid in a rotationally symmetric cylindrical container under the effect of surface and gravitational forces. We consider a right circular cylinder, oriented vertically, with a concave spheroidal bottom, for the case in which there is not sufficient liquid to cover the bottom entirely. This is the same configuration for which a stability study was carried out in [1]. Numerical results are obtained for a container currently used for the storage of liquid fuels in National Aeronautics and Space Administration Centaur space vehicles, for which the axial ratio of the bottom is $b/a = 0.724$. A vertical cross section of the cylinder and liquid is shown in Figure 1.

Equations describing the sloshing motion of liquids in rotationally symmetric containers are derived in [2] using a surface-normal polar coordinate system particularly suited to such problems. It is assumed there that the fluid flow is irrotational and incompressible and the free-surface boundary conditions are obtained from the time-dependent Bernoulli equation and the kinematic equation. The difference in pressure across the free surface at any point, due to the interfacial surface tension, is proportional to the mean curvature at that point. The edges of the surface satisfy time-independent contact angle conditions with the container bottom and the cylinder wall. We follow the derivation in [2] for obtaining the equations of motion for the case studied here, but we use a different technique for obtaining the numerical solution.

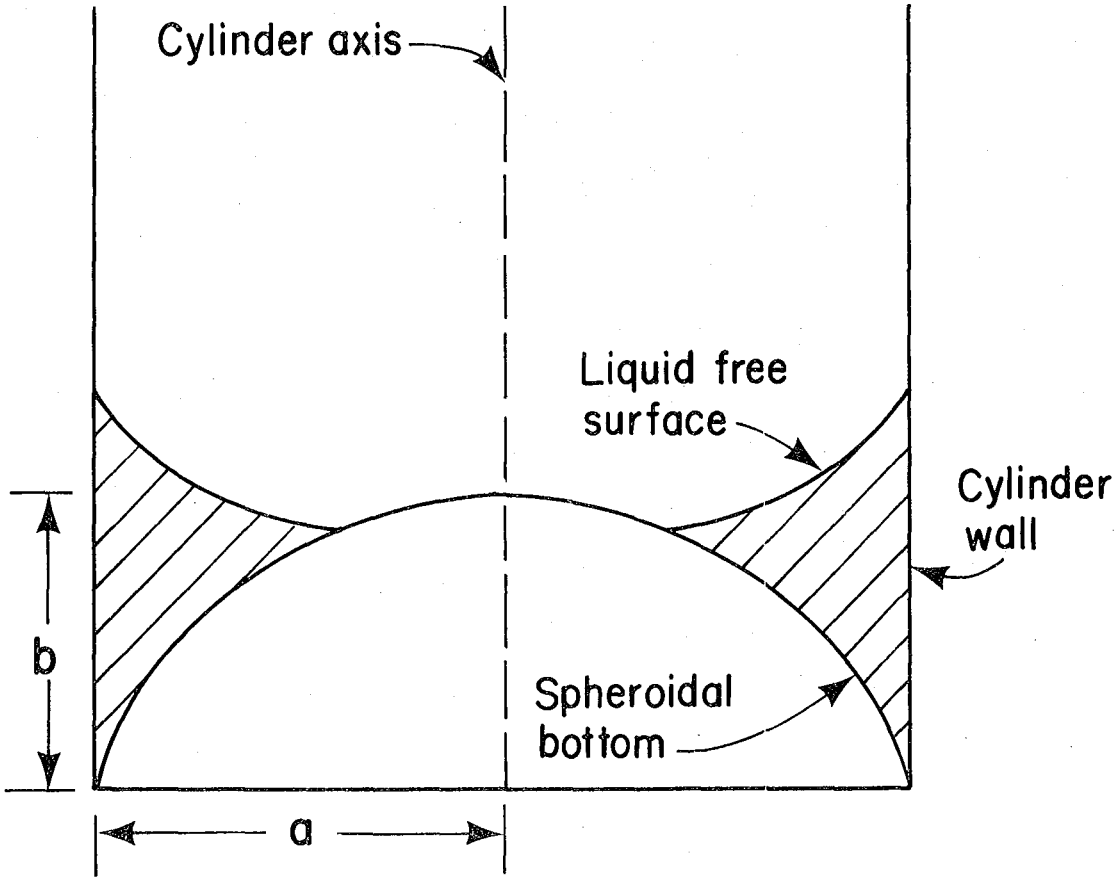

Figure 1. Vertical cross section of the cylinder and liquid.

XBL 781-103

2. Scaled Variables

We consider a circular cylindrical coordinate system with the z axis along the cylinder's axis of symmetry. It is convenient to define scaled length and time variables. Let symbols with a bar over them denote the corresponding physical, unscaled variables. Let

$$r = \bar{r}/a$$

$$z = \bar{z}/a$$

$$t = \bar{t}\,[(1+|B|)\,\sigma/\rho a^3]^{1/2}$$

$$H = \bar{H}\,a$$

$$B = \kappa a^2 = \rho g a^2/\sigma$$

$$2H_o = (p_g - p_o)\,a/\sigma$$

where a, the cylinder's radius, is the characteristic length used for scaling, t is the time, ρ is the difference in densities between the liquid and gas phases, g is the acceleration due to gravity, considered positive when directed vertically downward, σ is the gas-liquid surface tension, κ is the capillary constant, B is the Bond number, H is the mean curvature at a point on the free surface, considered negative when the surface is concave upward, p_g is the gas pressure, and p_o is the liquid static pressure at the height $z = 0$.

The difference in pressure across the free surface satisfies the equation

$$p - p_g = -\,2H\,\sigma/a\ .$$

The liquid static pressure is given by

$$p - p_o = -\,\rho g z a\ .$$

From these equations it follows that the curvature H at any point on the equilibrium free surface is related to H_o, B, and z by

$$2H = 2H_o + Bz\ .$$

3. Equilibrium Free Surface

We consider the vertical cross section through the axis of the cylinder shown in Figure 2. The cross section of the liquid is bounded by three curves: the meridians along the free surface, the cylinder wall, and the container bottom. Let s be the arc length along this boundary, increasing clockwise. Let $s = 0$ be the intersection of the meridians on the free surface and the bottom, and let $s = S$ be the intersection of the meridians on the free surface and the cylinder wall.

The equilibrium free surface is rotationally symmetric about the axis of the cylinder. Its height is a function of r only and not of Θ. Thus the equilibrium surface can be described parametrically by the equations

$$r = R(s) \quad \text{and} \quad z = Z(s)$$

for $0 \leqslant s \leqslant S$ and $0 \leqslant \Theta < 2\pi$. Let ψ be the angle in the cross-sectional plane between the tangent at a point on the free surface and the horizontal. Let ψ be positive when the surface slopes upward in the direction of increasing s. Then

$$\tan \psi = Z_s/R_s ,$$

where the subscript s denotes d/ds. Let the spheroidal bottom be described by

$$z = Z_B(r)$$

for $R(0) \leqslant r \leqslant 1$ and $0 \leqslant \Theta \leqslant 2\pi$. Let χ denote the angle in the cross-sectional plane between the tangent at a point on the bottom and the horizontal. Let χ be negative when the bottom slopes downward in

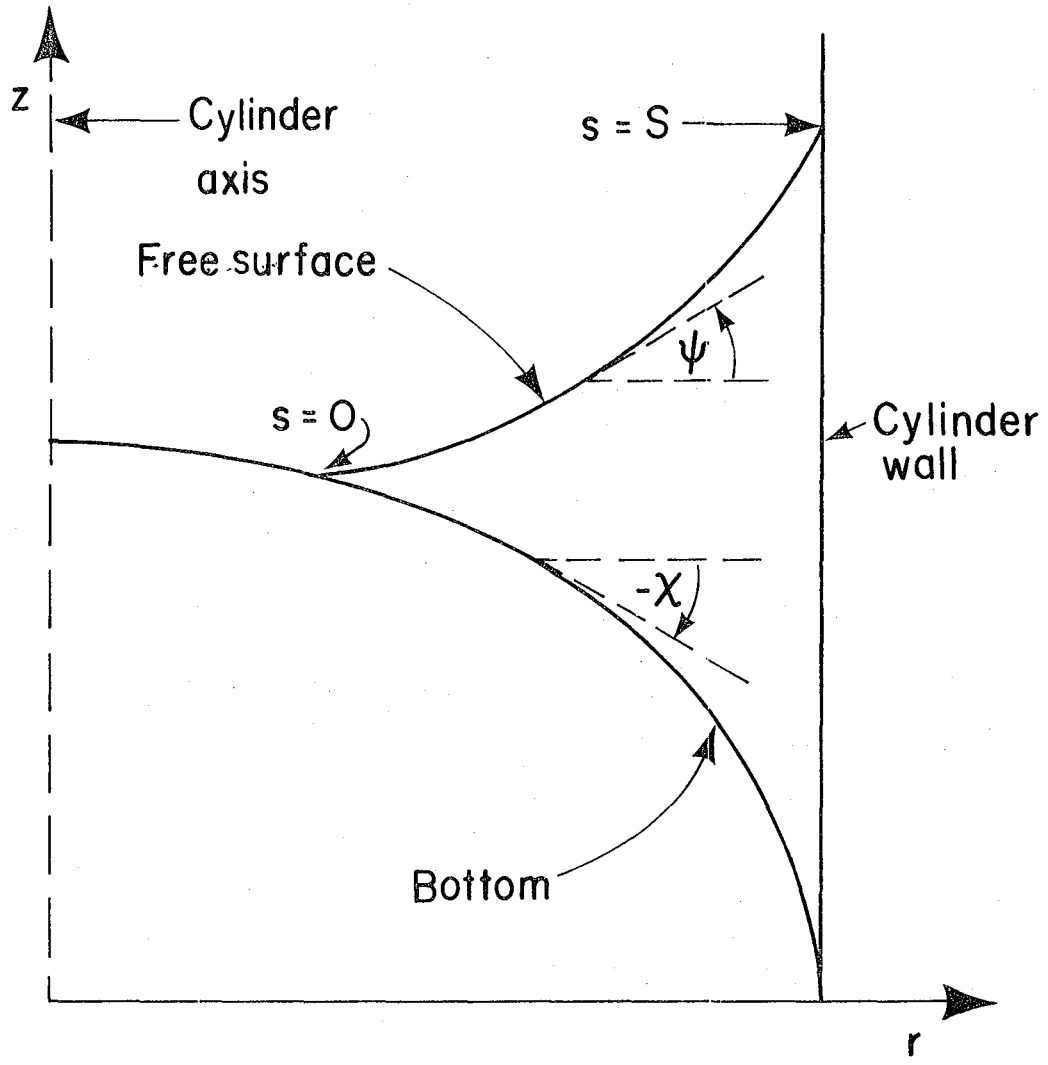

Figure 2. Vertical cross section of the liquid showing coordinates.

XBL 781-102

the direction of increasing r, as it does in our case. Then

$$\tan \chi = \frac{d}{dr} Z_B(r) .$$

The equilibrium free surface is the solution of the time independent Bernoulli equation,

$$\psi_s = 2H_o + BZ - (\sin \psi)/R , \tag{3.1}$$

with

$$R_s = \cos \psi \tag{3.2}$$

$$Z_s = \sin \psi, \tag{3.3}$$

subject to the contact conditions,

$$Z(s) = Z_B(R(s)) \quad \text{at } s = 0 \tag{3.4}$$

$$R(s) = 1 \quad \text{at } s = S \tag{3.5}$$

(the scaled radius of the cylinder is 1), and subject to the contact angle conditions,

$$\psi - \chi = \gamma \text{ at } s = 0 \tag{3.6}$$

$$\pi/2 - \psi = \gamma \text{ at } s = S , \tag{3.7}$$

where γ is the contact angle. The volume of the liquid in the cylinder is

$$V = 2\pi \int_0^S [Z(s) - Z_B(R(s))]R(s) \cos \psi(s) \, ds . \tag{3.8}$$

This last equation determines implicitly the value of H_o of V is given.

Equations (3.1) - (3.8) are the equations for the equilibrium free surface. The solution of these equations varies with the volume, the Bond number, the contact angle, and the shape of the bottom of the container. Depending on the values of these parameters, there may be

no, one, or more solutions of these equations [1]. If the equilibrium surface exists, it may be stable or unstable to small perturbations.

These equations are solved by the program CAPIL [3]. This program uses PASVA2 [4], a general-purpose finite difference solver for non-linear first-order systems of differential equations subject to two-point boundary conditions. PASVA2 solves these equations by iterating from an initial approximation to the surface. Either the user can supply the initial approximation, or the subroutine CYLCUR can generate it. When making calculations with the same fill for a sequence of Bond numbers, we let CYLCUR generate the initial approximation for the first case and use the output of each case as the initial approximation for the next case.

4. Small-Amplitude Periodic Sloshing Modes of the Liquid

The sloshing motion is treated as potential flow in an incompressible fluid. The fluid velocity v at any point is the gradient of a potential function $\tilde{\phi}$

$$v = \nabla\tilde{\phi} \ .$$

Since the fluid is incompressible, $\nabla\cdot v = 0$, so $\tilde{\phi}$ satisfies Laplace's equation

$$\Delta\tilde{\phi} = 0 \ . \tag{4.1}$$

The boundary condition on $\tilde{\phi}$ along the cylinder wall and the bottom is

$$\tilde{\phi}_n = 0 \ , \tag{4.2}$$

where the subscript n denotes the outward normal derivative.

The displacement of the free surface from its equilibrium will be described in surface polar normal coordinates s , Θ and η . The coordinate s is the arc length along the equilibrium surface, and the coordinate η is the displacement normal to this surface [1]. The perturbed surface is described by

$$\eta = \tilde{H}(s,\Theta,t) \ .$$

The time-dependent Bernoulli equation is linearized in the perturbation $\tilde{H}$. Since $\tilde{H}_t$ is the component of fluid velocity normal to the equilibrium surface, $\tilde{H}$ and $\tilde{\phi}$ are related by the kinematic equation on the eqiulibrium surface

$$\tilde{\phi}_n = \tilde{H}_t \ . \tag{4.3}$$

This is the boundary condition on $\tilde{\phi}$ along the free surface; it depends on the unknown function $\tilde{H}$.

The sloshing motion will be analyzed in terms of normal modes

$$\tilde{\phi} = \phi(r,z)\ \cos(m\theta)\ \cos(\omega t)\ ,$$

$$\tilde{H} = H(s)\ \cos(m\theta)\ \sin(\omega t)\ .$$

Equation (4.3) can be used to eliminate the function $\tilde{H}$ from the linearized time-dependent Bernoulli equation. The result is

$$-\ (R\phi_{ns})_s + RQ(s)\phi_n = \omega^2(1+|B|)R\phi\ , \tag{4.4}$$

where

$$Q(s) = BR_s + (m/R)^2 - [\psi_s{}^2 + (Z_s/R)^2]\ . \tag{4.5}$$

The solution of differential equation (4.3) gives the boundary condition on ϕ along the equilibrium surface. The boundary condition is specified by the contact angle conditions at $s = 0$ and $s = S$, which are assumed to be time independent. The perturbed surface and the equilibrium surface must have the same contact angle with the cylinder wall and the bottom.

These conditions relate H_s, ψ_s, and χ_r at $s = 0$ and $s = S$. In terms of the function ϕ these conditions are

$$\phi_{ns} \sin\gamma - \phi_n\ (\psi_s \cos\gamma - \chi_r \cos\chi) = 0 \quad \text{at} \quad s = 0 \tag{4.6}$$

$$\phi_{ns} \sin\gamma + \phi_n\psi_s \cos\gamma = 0 \quad \text{at} \quad s = S\ . \tag{4.7}$$

Equations (4.1), (4.2), and (4.4) - (4.7) determine the eigenfunctions ϕ and the corresponding eigenvalues ω.

It will be convenient to let $\theta 0$, $\theta 1$, $\theta 2$, ... denote normal modes having $\cos(m\theta)$ dependence with the values $m = 0, 1, 2, \ldots$, respectively. We also shall let R0, R1, R2, ... denote normal modes having 0, 1, 2, ... radial nodes in the interval $0 < s < S$ (not counting the nodes, if any, at the endpoints of the interval).

5. Discrete Representation and the Solution of Laplace's Equation

The functions ϕ and ϕ_n on the boundary of the vertical cross section of the liquid will be represented by their values at $N + M$ points

$$\Phi = (\phi(s_1), \phi(s_2), \ldots, \phi(s_{N+M}))$$

and similarly for Φ_n. These points are shown in Figure 3. The first N of these points will be along the meridian of the free surface in the cross-sectional plane. The remaining M will be on the meridians of the cylinder wall and the bottom in the cross-sectional plane. None of the s_j are corner points of the boundary.

We shall partition the vectors Φ and Φ_n into two parts: Φ_1 includes values of ϕ at points on the free surface, and Φ_2 includes those on the cylinder wall and the bottom

$$\Phi = (\Phi_1, \Phi_2)$$

$$\Phi_1 = (\phi(s_1), \phi(s_2), \ldots, \phi(s_N))$$

$$\Phi_2 = (\phi(s_{N+1}), \ldots, \phi(s_{N+M})) .$$

The boundary condition on ϕ along the cylinder wall and the bottom, Equation (4.2), becomes

$$\Phi_{2n} = 0 . \tag{5.1}$$

Because $\tilde{\phi}$ satisfies Laplace's equation, Green's formula yields an integral equation that relates ϕ and ϕ_n on the boundary of the vertical cross section of the liquid. This can be approximated by a matrix equation of the form:

$$W\Phi = C\Phi_n . \tag{5.2}$$

The calculation of the matrices W and C is described in [5].

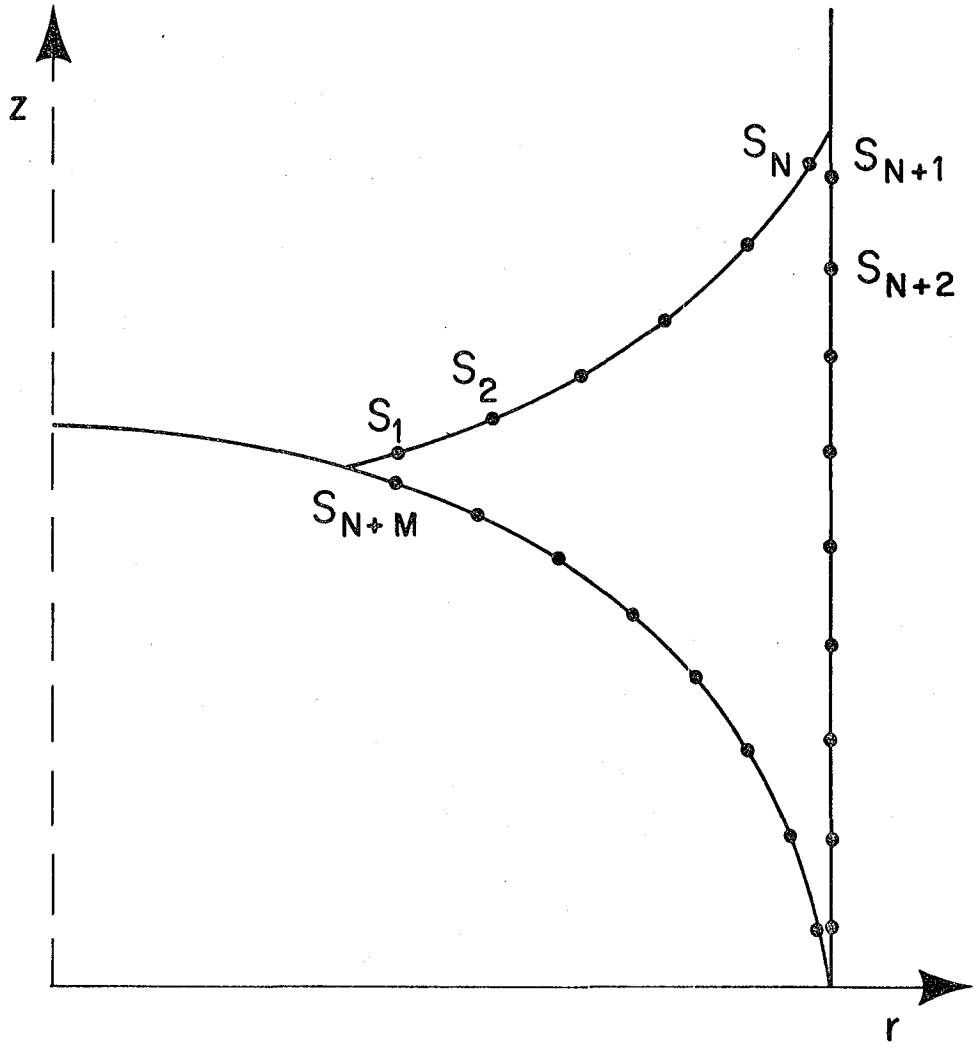

Figure 3. The discrete set of points on the boundary.

XBL 781-104

6. Discrete Representation of the Boundary Condition on the Free Surface

Using Equation (4.4) and the contact angle conditions (4.6) and (4.7), we will derive a discrete set of equations relating ϕ and ϕ_n at the points $s_1, s_2, \ldots s_N$ along the meridian of the free surface in the cross-sectional plane. Let this meridian be divided into N intervals. The j^{th} interval has

$$t_j \leqslant s \leqslant t_{j+1} ,$$

where $t_1 = 0$ and $t_{N+1} = S$. Let s_j be the midpoint of the j^{th} interval.

We integrate Equation (4.4) over the j^{th} interval

$$R(t_j)\phi_{ns}(t_j) - R(t_{j+1})\phi_{ns}(t_{j+1}) + \int_{t_j}^{t_{j+1}} Q(s)R(s)\phi_n(s)\, ds$$

$$= \omega^2(1+|B|) \int_{t_j}^{t_{j+1}} R(s)\phi(s)\, ds . \qquad (6.1)$$

The integrals are approximated by

$$\phi_n(s_j) \int_{t_j}^{t_{j+1}} Q(s)\, R(s)\, ds$$

and

$$\phi(s_j) \int_{t_j}^{t_{j+1}} R(s)\, ds .$$

If t_j is not an endpoint of the meridian, we approximate $\phi_{ns}(t_j)$ by

$$\phi_{ns}(t_j) \approx \frac{\phi_n(s_j) - \phi_n(s_{j-1})}{s_j - s_{j-1}} .$$

Substituting these approximations into Equation (6.1) gives

$$T_{j-1,j}\,\phi_n(s_{j-1}) + T_{jj}\phi_n(s_j) + T_{j,j+1}\phi_n(s_{j+1}) = \omega^2 A_{jj}\phi(s_j) , \quad (6.2)$$

where

$$A_{jj} = (1+|B|) \int_{t_j}^{t_{j+1}} R(s)\ ds ,$$

$$P_j = \int_{t_j}^{t_{j+1}} Q(s)R(s)\ ds ,$$

$$T_{j,j+1} = -R(t_{j+1})/(s_{j+1}-s_j) ,$$

and

$$T_{jj} = -T_{j-1,j} - T_{j,j+1} + P_j .$$

For $t_1 = 0$, the inner endpoint of the meridian, we approximate

$$\phi_{ns}(t_1) \approx \frac{\phi_n(s_1) - \phi_n(t_1)}{s_1 - t_1} .$$

To eliminate the unknown $\phi_n(t_1)$, we use the contact angle condition (4.6)

$$\phi_{ns}(t_1) \sin\gamma = L_1\,\phi_n(t_1) ,$$

where

$$L_1 = \psi_s(t_1)\cos\gamma - \chi_r(t_1)\cos\chi .$$

These give

$$\phi_{ns}(t_1) = K_1\,\phi_n(s_1) ,$$

where

$$K_1 = L_1 / [\sin\gamma + (s_1 - t_1)L_1] \ .$$

Substituting this approximation into Equation (6.1) gives

$$T_{11}\phi_n(s_1) + T_{12}\phi_n(s_2) = \omega^2 A_{11}\phi(s_1) \ , \tag{6.3}$$

where

$$T_{11} = -T_{12} + K_1 R(t_1) + P_1 \ .$$

For $t_{N+1} = S$, the outer endpoint of the meridian, we approximate

$$\phi_{ns}(t_{N+1}) \approx \frac{\phi_n(t_{N+1}) - \phi_n(s_n)}{t_{N+1} - s_N} \ .$$

To eliminate the unknown $\phi_n(t_{N+1})$, we use the contact angle condition (4.7)

$$\phi_{ns}(t_{N+1}) \sin\gamma = -L_2 \phi_n(t_{N+1}) \ ,$$

where

$$L_2 = \psi_s(t_{N+1}) \cos\gamma \ .$$

These give

$$\phi_{ns}(t_{N+1}) = -K_1 \phi_n(s_N) \ ,$$

where

$$K_2 = L_2 / [\sin\gamma + (t_{N+1} - s_n)L_2] \ .$$

Substituting this approximation into Equation (6.1) gives

$$T_{N-1,N}\phi_m(s_{N-1}) + T_{NN}\phi_n(s_N) = \omega^2 A_{NN}\phi(s_N), \tag{6.4}$$

where

$$T_{NN} = -T_{N-1,N} + K_2 R(t_{N+1}) + P_N \ .$$

Equations (6.2) - (6.4) can be written in matrix form as

$$T\Phi_{1n} = \omega^2 A \Phi_1 \quad . \tag{6.5}$$

This is the boundary condition on ϕ along the meridian on the free surface. A is diagonal, and the diagonal elements are positive. T is tridiagonal and symmetric, and the off-diagonal elements are negative.

The set of Equations (5.1), (5.3), and (6.5) is the discrete version of the eigenvalue problem for the small-amplitude, periodic sloshing modes of a liquid in a vertical, rotationally symmetric cylinder.

7. Numerical Solution of the Discretized Eigenvalue Problem

We write the matrices W and C of equation (5.3) in block form: W_{11}, W_{12}, W_{21}, W_{22}, and similarly for C. Subscript 1 denotes the rows and columns corresponding to the N points along the free surface, and subscript 2 denotes those corresponding to the M points along the cylinder wall and bottom. Since Φ_{2n} is zero, Equation (5.3) can be written

$$\begin{aligned} W_{11}\,\Phi_1 + W_{12}\,\Phi_2 &= C_{11}\,\Phi_{1n}\ , \\ W_{21}\,\Phi_1 + W_{22}\,\Phi_2 &= C_{21}\,\Phi_{1n}\ . \end{aligned} \tag{7.1}$$

The matrix A is diagonal, so Equation (6.5) is easy to solve for Φ_1, which we can eliminate from Equations (7.1).

Define

$$\begin{aligned} F_{11} &= W_{11}\,A^{-1}\,T\ , \\ F_{21} &= W_{21}\,A^{-1}\,T\ . \end{aligned} \tag{7.2}$$

Then Equations (7.1) give

$$\begin{aligned} F_{11}\,\Phi_{1n} &= \omega^2(C_{11}\Phi_{1n} - W_{12}\Phi_2), \\ F_{21}\,\Phi_{1n} &= \omega^2(C_{21}\Phi_{1n} - W_{22}\Phi_2)\ . \end{aligned} \tag{7.3}$$

Equations (7.3) can be written as single matrix equation for the eigenvector (Φ_{1n},Φ_2)

$$\begin{pmatrix} F_{11} & 0 \\ F_{21} & 0 \end{pmatrix} \begin{pmatrix} \Phi_{1n} \\ \Phi_2 \end{pmatrix} = \omega^2 \begin{pmatrix} C_{11} & -W_{12} \\ C_{12} & -W_{22} \end{pmatrix} \begin{pmatrix} \Phi_{1n} \\ \Phi_2 \end{pmatrix}\ . \tag{7.4}$$

Equation 7.4 could be solved for the eigenvalues ω^2; however, M of the eigenvectors have the eigenvalue $\omega^2 = 0$. A linearly independent

set of these eigenvectors is

$$\Phi_{1n} = 0 \qquad \Phi_2 = e_j \qquad j=1,2,\ldots M,$$

where e_j is the vector with a one in the j^{th} position and zeros elsewhere. These eigenvectors correspond to no motion of the free surface, since Φ_{1n} is zero. A computer program that calculates all the eigenvalues of a matrix, such as the IMSL routine EIGZF, will waste some time computing these unwanted eigenvalues.

We can avoid calculating the zero eigenvalues by eliminating Φ_2 from the pair of Equations (7.3). Define

$$D = C_{11} - W_{11} W_{22}^{-1} C_{21} ,$$

$$E = F_{11} - W_{12} W_{22}^{-1} F_{21} = (W_{11} - W_{12} W_{22}^{-1} W_{21})A^{-1}T \quad . \tag{7.5}$$

Then Equations (7.3) combine to give

$$E\Phi_{1n} = \omega^2 D\Phi_{1n} \tag{7.6}$$

Equation (7.6) can be solved for its eigenvalue by the IMSL routine EIGZF, which uses a QZ algorithm to reduce E to upper Hessenberg form and D to upper triangular form.

The solution of Equation (7.6) is performed by the program SLOSH. The input to SLOSH is the set of points describing the equilibrium free surface calculated by CAPIL and parameters that define the cylinder wall and spheroidal bottom. SLOSH then calculates the matrices A, T, W, and C; uses the IMSL routine LINV1F to calculate W_{22} inverse; calculates the matrices D and E; and uses EIGZF to calculate the eigenvalues. This method of solving the eigenvalue equation is not the most computationally efficient, but by using

the existing and reliable IMSL routines it requires the least amount of programming effort.

For comparison, the routine EIGZF was used to solve both Equation (7.6) and Equation (7.4) for a few cases. The numerical values of corresponding eigenvalues for these two methods were identical to the four figures that were printed out in each case.

8. Small-Amplitude Periodic Sloshing Modes of the Liquid between Two Concentric Right Circular Cylinders

In this section we solve the eigenvalue problem for the small-amplitude, periodic sloshing modes of the liquid contained between two concentric, vertically oriented, right circular cylinders of radii r_0 and r_1. A cross section is shown in Figure 4. The equilibrium surface is a horizontal plane when the contact angle is 90^o. The normal mode problem for this case has an analytic solution. We can use this solution to test the accuracy of the program SLOSH.

Let $\mathcal{D}$ be the rectangular domain $r_0 \leq r \leq r_1$ and $0 \leq z \leq z_0$. Laplace's Equation for ϕ in the domain $\mathcal{D}$ is

$$\phi_{rr} + \frac{1}{r}\phi_r + \phi_{zz} - \frac{m^2}{r^2}\phi = 0 \ . \tag{8.1}$$

The boundary conditions are

$$\phi_r = 0 \qquad \text{at } r = r_0 \text{ and } r_1 \ ,$$

$$\phi_r = 0 \qquad \text{at } z = 0 \ .$$

Equation (4.4) for ϕ on the free surface, $z = z_0$, is

$$-\frac{1}{r}(r\phi_{rz})_r + Q(r)\phi_z = \omega^2(1+|B|)\phi \ , \tag{8.2}$$

where

$$Q(r) = B + (m/r)^2 \ .$$

The contact angle conditions, Equations (4.6) and (4.7), become

$$\phi_{rz} = 0 \qquad \text{at } (r_0,z_0) \text{ and } (r_1,z_0) \ .$$

We solve these equations by separation of variables. Let

$$\phi(r,z) = X(r)\,U(z)$$

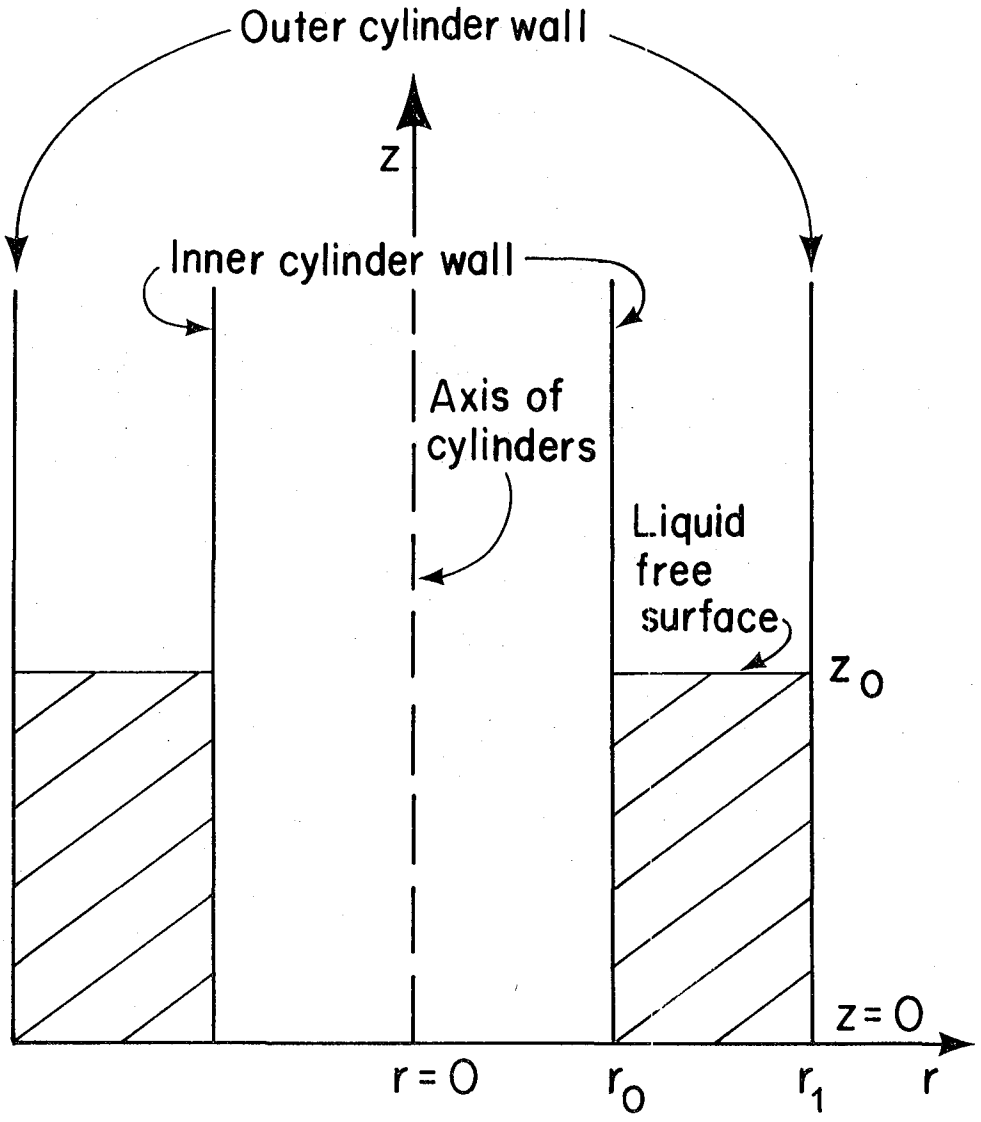

Figure 4. Cross section of two concentric cylinders or radii r_0 and r_1, respectively.

XBL 781-105

then (8.1) gives the pair of equations

$$U'' = k^2 U \tag{8.3}$$

$$X'' + \frac{1}{r} X' + (k^2 - m^2/r^2)X = 0 \ , \tag{8.4}$$

with boundary conditions

$$U' = 0 \text{ at } z = 0 \ , \tag{8.5}$$

$$X' = 0 \text{ at } r = r_0 \text{ and } r_1 \ . \tag{8.6}$$

The contact angle conditions will be automatically satisfied if Equation (8.6) is satisfied.

Equation (8.2) gives an equation for the eigenvalue

$$\omega^2 = \frac{(k^2 + B)}{(1 + |B|)} \quad \frac{U'(z_0)}{U(z_0)} \ .$$

The solution of (8.3) and (8.5) is

$$U = \cosh (kz) \ .$$

Thus the eigenvalue is

$$\omega^2 = \frac{k(k^2 + B)}{(1 + |B|)} \quad \tanh (kz_0) \ . \tag{8.7}$$

The solution of (8.4) is

$$X(r) = c \, J_m(kr) + d \, Y_m(kr) \ ,$$

where J_m and Y_m are Bessel functions of the first and second kind of order m. Equation (8.6) requires

$$c \, J_m'(kr_0) + d \, Y_m'(kr_0) = 0 \ ,$$

$$c \, J_m'(kr_1) + d \, Y_m'(kr_1) = 0 \ .$$

These will have a nontrivial solution for c and d if

$$J_m'(kr_1) \, Y_m'(kr_0) - J'_m(kr_0) \, Y'_m(kr_1) = 0 \ . \tag{8.8}$$

Equation (8.8) gives the values of k for the normal modes. The first few values for the case $r_0 = 0.5$ and $r_1 - 1.0$ are listed in Table 1 to the accuracy indicated.

Table 1. k values for m = 0, 1, and 2.

m = 0	m = 1	m = 2
0.0	1.3547	2.6812
6.3932	6.5649	7.0626
12.6247	12.7064	12.9494
18.8889	18.9427	19.1032
25.1624	25.2045	25.3224

The solution m = 0, k = 0.0 corresponds to no movement of the equilibrium surface or of the liquid.

9. Comparison of the Analytically and Numerically Calculated Solutions for the Normal Modes of the Liquid between Two Cylinders

Figure 4 shows the cross section of a liquid contained between two concentric right circular cylinders, oriented vertically. Each of the four sides of the cross section (the free surface, the bottom, and the two cylinder walls) was divided into n intervals of equal length. The velocity potential ϕ on the perimeter of the cross section was represented by its values at the midpoints of these $4n$ intervals. These $4n$ values of ϕ are related by Equations (5.1), (5.3), and (6.5). Numerical solutions of these equations were computed for the case $r_0 = 0.5$, $r_1 = 1.0$, $z_0 = 0.9$, contact angle 90^o, and Bond number 0 using the program SLOSH.

Numerically calculated squares of the frequencies for the modes θ1RO, θ1R1, and θ1R2 using n = 5, 10, and 20 points are shown in Table 2. The corresponding analytic values for the squares of the frequencies, calculated from Equation (8.7) and the k values of Table 1, are also shown.

Table 2. Squares of frequencies for various normal modes

	θ1RO	θ1R1	θ1R2
5 points	2.157	292.1	1965.
10 points	2.127	284.8	2080.
20 points	2.118	280.7	2072.
analytic	2.087	282.9	2052.

The relative errors of the numerically calculated squares of the frequencies $[\omega^2(\text{n points}) - \omega^2(\text{analytic})]/\ \omega^2$ (analytic), are shown in Table 3.

Table 3. Relative errors of the squares of frequencies.

	θ1R0	θ1R1	θ1R2
5 points	0.034	0.033	-0.042
10 points	0.019	0.007	0.014
20 points	0.015	-0.008	0.010

Note that the relative errors of the <u>frequencies</u> are approximately half these values. The error decreases substantially between n = 5 and n = 10, but less so between n = 10 and n = 20. Even the errors for n = 5 are quite small, considering that only five radial modes can be represented by a 5-point approximation to the meridian on the free surface.

Numerically calculated squares of the frequencies for the modes θ0R0, θ0R1, θ0R2, θ2R0, θ2R1, and θ2R2 using n = 10 points are shown in Table 4. Corresponding analytic values are shown also.

Table 4. Squares of frequencies for various normal modes.

	θ0R0	θ0R1	θ0R2
10 points	$0.7\ \ 10^{-12}$	265.4	2038.
analytic	0.0	261.3	2012.
	θ2R0	θ2R1	θ2R2
10 points	19.99	346.6	2201.
analytic	18.97	352.3	2171.

The relative errors of these squares of frequencies are shown in Table 5.

Table 5. Relative Errors of the squares of frequencies.

	R0	R1	R2
Θ0 modes	--	0.016	0.013
Θ2 modes	0.054	-0.016	0.014

The relative errors of the squares of frequencies for n = 10 points, as shown in Tables 3 and 5, are typically from 0.01 to 0.02. These results show the program SLOSH calculates with satisfactory accuracy for our purposes the frequencies of the normal modes of a liquid contained between two concentric right circular cylinders.

10. Equilibrium Free Surfaces of a Liquid in a Vertical Right Circular Cylinder with a Concave Spheroidal Bottom

With a given volume of liquid in the cylindrical container we associate a dimensionless fill height defined as follows: let the given volume V equal the volume bounded by the container wall and bottom and the horizontal plane $z = z_v$. Then the fill height h_v is z_v divided by the container radius a.

$$h_v = z_v/a .$$

The axial ratio of the spheroidal bottom is $b/a = 0.724$.

Equilibrium free surfaces, approximated by 21 points on the meridian, were calculated by the program CAPIL for contact angle $\gamma = 0^o$ and for the fill heights: 0.20, 0.25, 0.30, 0.35, 0.40, 0.45, 0.50, 0.60, and 0.70. For each fill height equilibrium surfaces were calculated for a sequence of increasingly negative Bond numbers. The first surface for each fill height was calculated for Bond number $B = 0$. The initial approximation to this surface was generated by the subroutine CYLCUR. The equilibrium surface for each Bond number was used as the initial approximation to the surface for the next Bond number in that sequence.

The equilibrium surfaces that we have calculated are members of a family with two parameters B and h_v. Let B_{eq} denote the critical value of the Bond number for the nonexistence of equilibrium surfaces of this family for a given fill height. Let B_{crit} denote the critical value of the Bond number for the stability of equilibrium surfaces of this family for a given fill height. Stable equilibrium surfaces

exist for $B_{crit} \leq B$, unstable equilibrium surfaces exist for $B_{eq} \leq B < B_{crit} < 0$ if $B_{eq} \neq B_{crit}$, and no equilibrium surfaces of this family exist for $B < B_{eq}$. (Other equilibrium surfaces might exist, such as multiple-valued surfaces or surfaces with shapes very different from those of this family.) Concus and Karasalo showed that unstable equilibrium surfaces exist for B infinitesimally lower than B_{crit} and $h_v < h_v^* = 0.503$, but that no equilibrium surfaces of this family exist for $B < B_{crit}$ and $h_v \geq h_v^*$ [1]. Their result may be restated as $B_{eq} < B_{crit}$ for $h_v < h_v^*$, but $B_{eq} = B_{crit}$ for $h_v \geq h_v^*$. Our calculations agree with their result and provide an estimate of B_{eq}.

For each fill height we found a Bond number B_{div}, depending on h_v, for which the iteration for the equilibrium surface diverged. The iteration using B_{div} was approached by a sequence of calculations using small decreases in B. Let B_{conv} denote the Bond number immediately preceding B_{div} in that sequence, $B_{div} < B_{conv} < 0$. For $B \geq B_{conv}$ the equilibrium surface changed only slowly with B. The equilibrium surface for each value of B was an excellent approximation to that for the next value of B in the sequence. This indicates that the divergence for the case B_{div} was caused not by the initial approximation but by the nonexistence of an equilibrium surface for this family. Thus B_{div} is an approximation to B_{eq}. Table 6 shows B_{conv} and B_{div} as a function of h_v. It also shows B_{crit} calculated to four decimal places by Concus and Karasalo [1].

Table 6. B_{conv}, B_{div}, and B_{crit} for various fill heights.

h_v	$-B_{conv}$	$-B_{div}$	$-B_{crit}$
0.20	1310.	1320.	480.4283
0.25	488.	492.	238.6539
0.30	216.	218.	132.9638
0.35	107.	108.	79.6741
0.40	58.0	58.2	49.9096
0.45	33.4	33.6	31.9190
0.50	20.2759	20.2760	20.2759
0.60	8.42	8.43	8.4411
0.70	3.98	3.99	4.0020

The data of Table 6 are shown in Figure 5. The solid line is the graph of B_{crit} and the dashed line is that of B_{div}. These lines divide the Bond-number, fill-height parameter space into three regions: one for which stable equilibrium surfaces exist, one for which unstable equilibrium surfaces exist, and one for which no equilibrium surfaces exist. (Growth rates for perturbations of the unstable equilibrium surfaces were calculated by the program SLOSH for various values of B and h_v. These will be discussed in the next section of this report.)

Figure 5 also shows data points from stability experiments carried out at the NASA Lewis Zero Gravity Facility for the container shown in Figure 1 [6]. The experiments used three containers with radii 7 cm, 5.5 cm, and 2 cm, respectively. In the experiment the container had

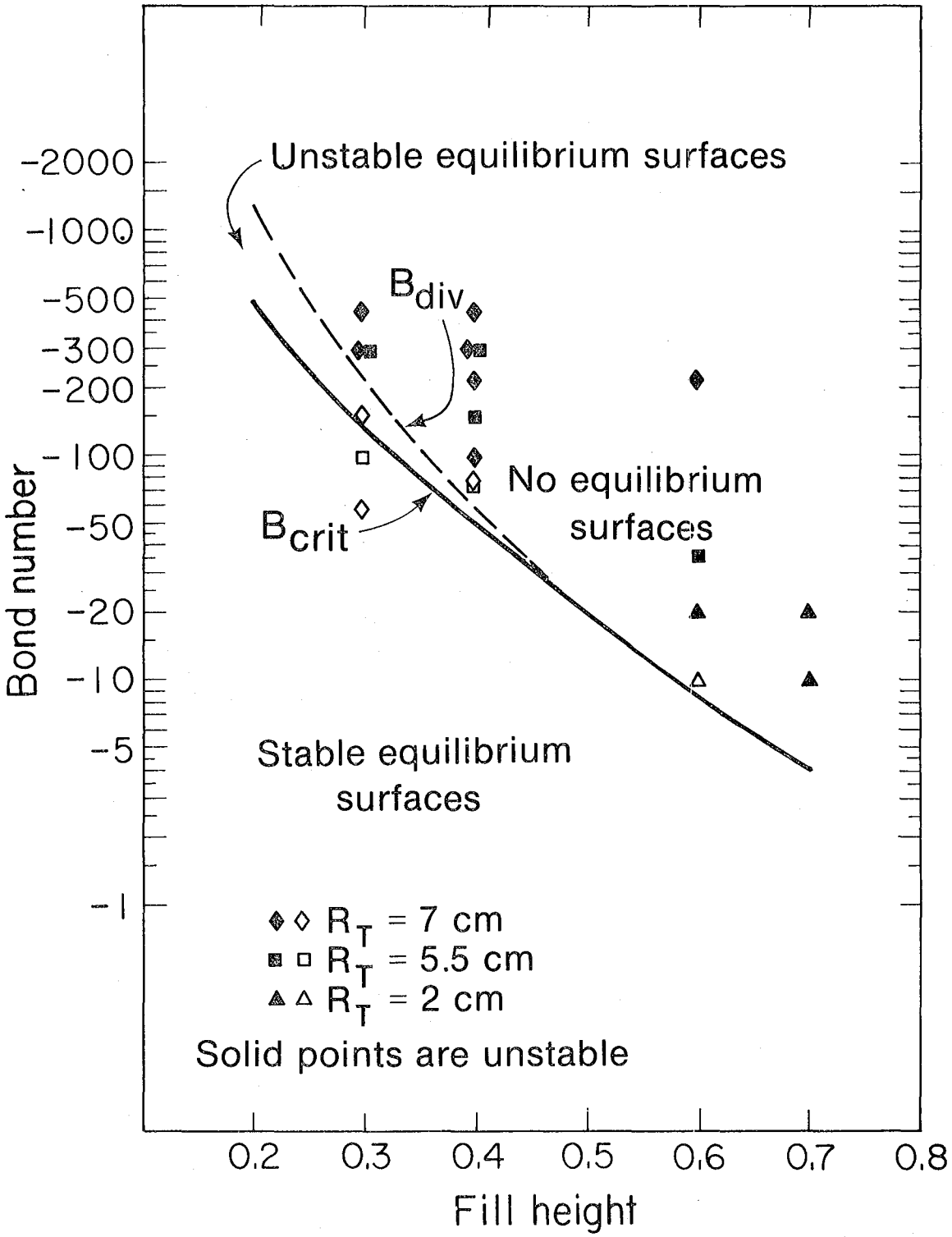

Figure 5. B_{crit} and B_{div} as functions of fill height compared with experimental points.

approximately 2.5 sec of free fall followed by approximately 2.5 sec of negative low-g fall. During the first 2.5 sec the liquid surface adjusts from one g to zero g. During the next 2.5 sec instabilities may be observed if they grow sufficiently rapidly. Solid data points correspond to experimental parameter values for which the surface was observed to be unstable. Open data points correspond to parameter values for which the surface did not develop a noticeable instability within the 2.5-sec time interval. The experimental data and the numerically calculated curves agree quite well. All the experiments in which the surface was observed to be unstable have Bond numbers $B < B_{crit} < 0$.

B_{div} is an approximation to B_{eq}. The accuracy of this approximation can be investigated by considering the cases $h_v = 0.60$ and 0.70. For $h_v = 0.60$ CAPIL diverges for some Bond number in the range $(-8.42, -8.43)$ and $B_{eq} = -8.4411$. The relative error in this case is less than 0.003. For $h = 0.70$ CAPIL diverges for some Bond number in the range $(-3.98, -3.99)$ and $B_{eq} = -4.0020$. The relative error in this latter case is less than 0.005.

From this we infer that the correct value of B_{eq} for $h_v = 0.50$ is slightly less than the value found here for the 21 point surfaces, and that there is a small range of Bond numbers between B_{crit} and B_{eq} for this value of h_v. This is supported by a calculation of the frequencies of individual normal modes, which is discussed in the next two sections. Based on an approximate calculation of the frequencies, the R0θ1 mode becomes marginally stable at $B = -20.243$, while all the other modes approach instability as B approaches -20.276.

11. Frequencies of the Normal Modes of a Liquid in a Vertical Right Circular Cylinder with a Concave Spheroidal Bottom

The frequencies of the small-amplitude periodic sloshing modes of a liquid in a vertical right circular cylinder with a concave spheroidal bottom were calculated by the program SLOSH for contact angle $\gamma = 0°$. The axial ratio of the spheroidal bottom is $b/a = 0.724$. The equilibrium free surfaces were approximated by 21 points of the meridian, as described in Section 10. These 21 points were the endpoints and midpoints of 10 intervals on the meridian. The velocity potential ϕ for perturbations to these surfaces was represented by its value at the 10 midpoints of these intervals, by its value at 10 points on the meridian on the cylinder wall, and at 10 points on the meridian on the bottom. We shall refer to this as the 10-point approximation to ϕ . Surfaces corresponding to numerous values of h_v and B were used.

A few surfaces approximated by 41 points on the meridian were used to check the accuracy of the frequencies calculated using the 21 point surfaces. For these cases ϕ was represented by its value at 20 points each on the meridians on the free surface, the cylinder wall, and the bottom. We shall refer to this as the 20-point approximation to ϕ .

The squares of frequencies for various normal modes and for various values of h_v and B calculated by SLOSH using the 10-point approximation are shown in Tables A 1 through A 11. Typically the values of ω^2 in these tables have a relative error of 1-2% for values of ω^2 that are not too small and for Bond numbers that are not

too near B_{div} . This will be discussed in more detail in Section 12.

These squares of frequencies are plotted as functions of B in Figures 6-12 for $h_v = 0.20, 0.30, \ldots 0.70$. Note that in Figures 10-12 ($h_v = 0.50 - 0.70$) a different scale for ω^2 is used for each mode that is plotted. The purpose is to show that all these modes have a similar dependence of ω^2 on B . However, in Figures 6-9 ($h_v = 0.20 - 0.40$) all the RO modes (ROθ1, ROθ2, ROθ3, ...) that are plotted in a given figure use the same scale for ω^2 . This is to show for each value of B which mode is most negative.

We shall first describe the general features of these figures, and then consider numerical details for particular cases and discuss the accuracy of the calculations.

Figure 6 shows graphs of $\omega^2(B)$ for the modes ROθ1, ROθ2, ROθ3, ROθ4, ROθ6, and R1θ0 for $h_v = 0.20$. The mode R1θ0 is plotted with a scale 1000 times that of the other modes. (An accuracy check shows the values for the R1θ0 mode are about 10% too large. However, we include it in Figure 6 for a rough comparison with the RO modes.) Note that the Bond numbers for which the various RO modes become marginally stable [for which $\omega^2(B) = 0$] lie in a small range.

Figure 7 shows this more clearly. The order in which the modes become unstable is as one would expect: First ROθ1 , then ROθ2 , ROθ3 , ROθ4 , and ROθ6 . (ROθ5 was not calculated for $h_v = 0.20$.) Note also that because the higher θ modes have steeper slopes ($d\omega^2/dB$), each mode, in turn, becomes the dominant unstable mode (most negative value of ω^2) for a short range of Bond numbers.

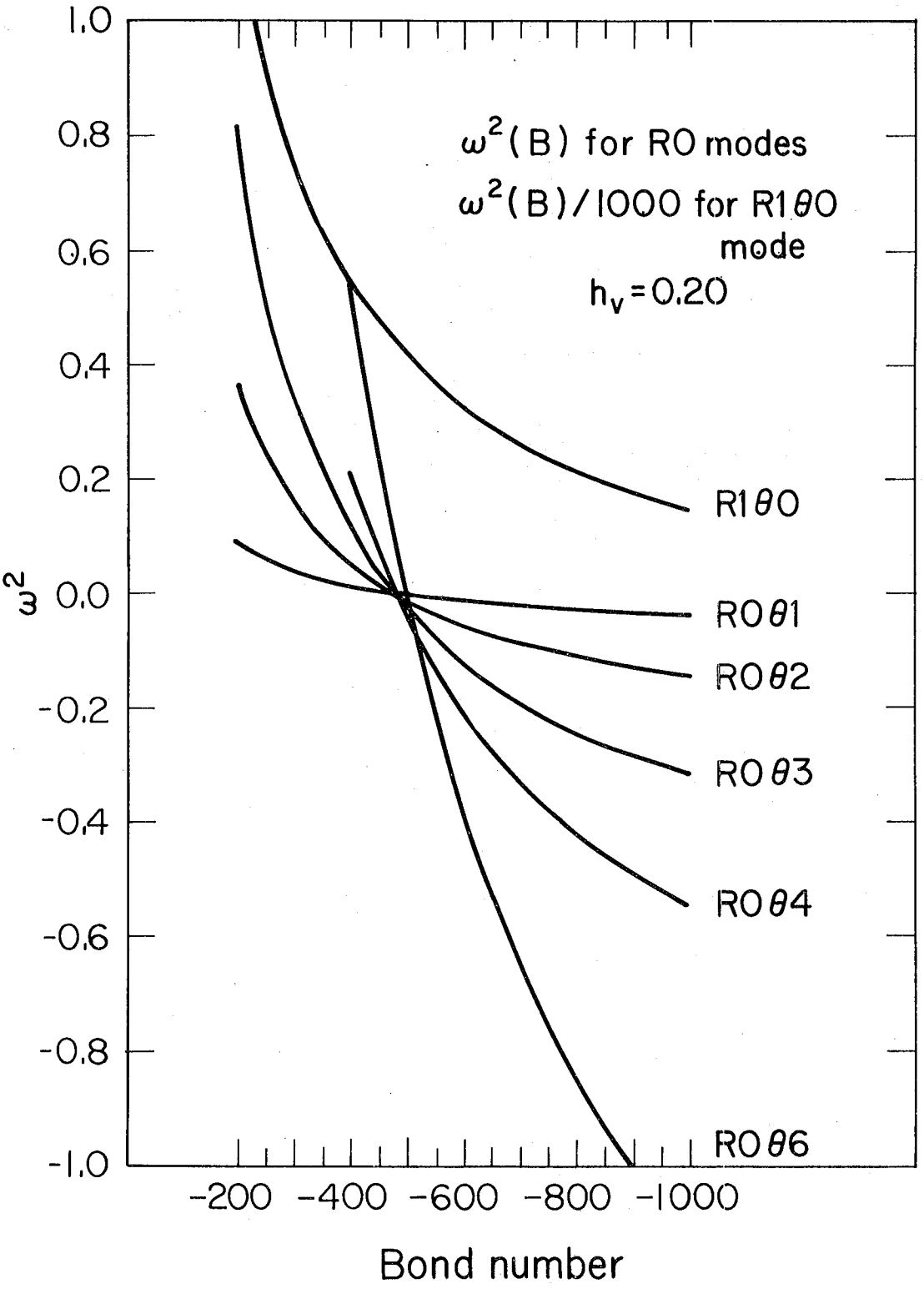

Figure 6. $\omega^2(B)$ of various modes for $h_v = 0.20$. XBL781-95

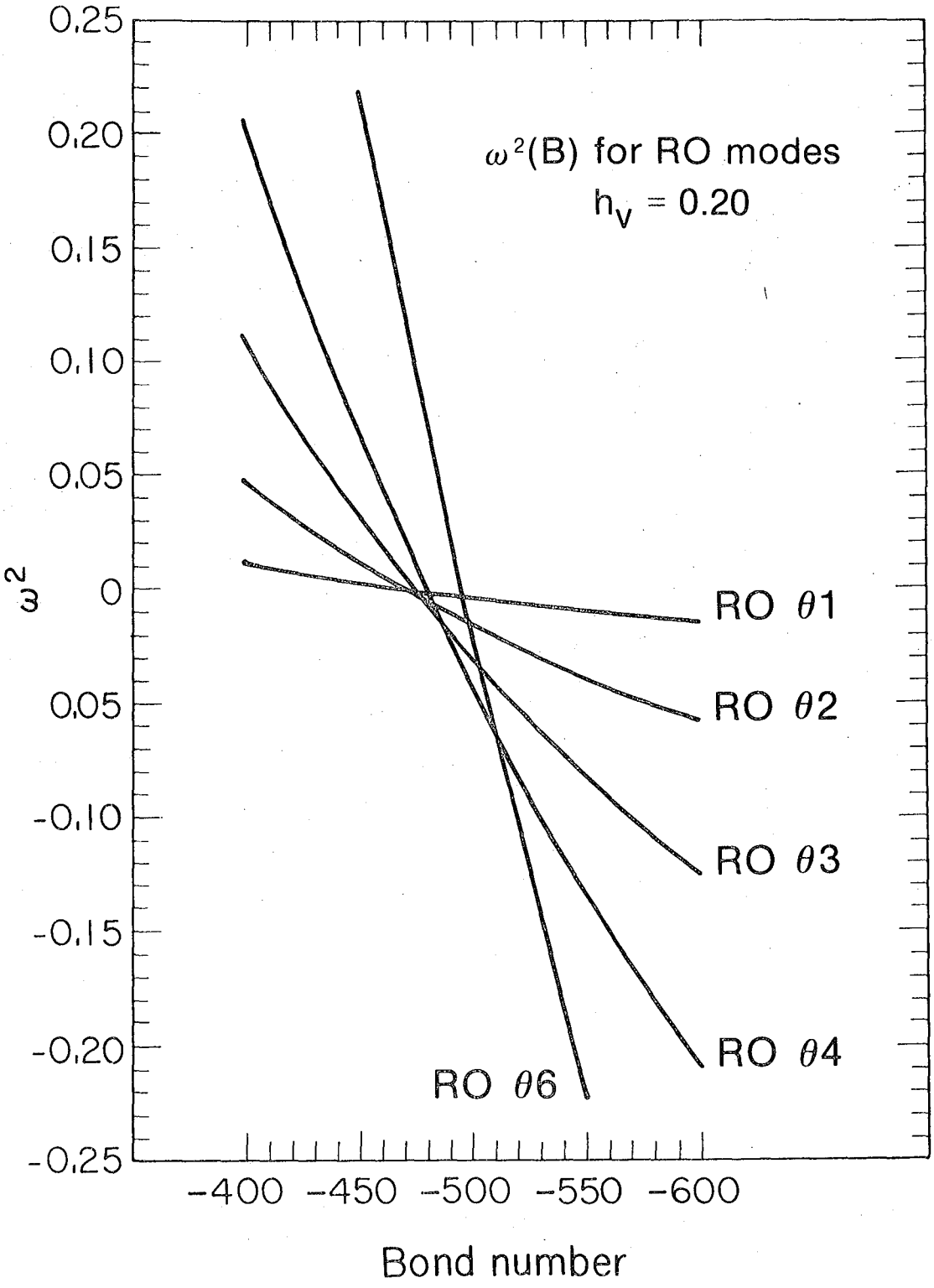

Figure 7. ω^2(B) of RO modes for h_v = 0.20 . XBL781-101

This same pattern for the R0 modes is shown in Figure 8 for $h_v = 0.30$. A new feature appears in this figure. It is that ω^2 for the R1θ0 mode passes through a point of inflection and begins to curve downward. The rate at which it approaches zero, the magnitude of $d\omega^2/d(B)$, increases as B approaches B_{div} . The functions $\omega^2(B)$ for the other R1 modes, R1θ1 to R1θ6 , have similar shapes and differ from that of R1θ0 by only a few percent, as shown in Table A 3. The functions $\omega^2(B)$ for the modes R2θ0 to R2θ6 have shapes similar to those for the R1 modes but magnitudes about five times larger. All the R1 and R2 modes curve downward as B approaches B_{div} .

Figure 9 shows that for $h_v = 0.40$ ω^2 becomes negative between B_{crit} and B_{conv} only for four modes: R0θ1 , R0θ2 , R0θ3 , and R0θ4 . Furthermore, only the first three modes become dominant instabilities in this range. The rate at which the R1θ0 mode approaches zero, $|d\omega^2/dB|$, becomes very great as B approaches B_{div} . Note also that $\omega^2(B)$ for each of the R0 modes passes through an inflection point and curves downward as B approaches B_{div} .

Figures 10, 11, and 12 are for the cases $h_v = 0.50$, 0.60 , and 0.70 , respectively. In each case the functions $\omega^2(B)$ for the various modes have similar shapes. They all curve downward for B near B_{crit} , and the rate at which they approach zero becomes very great as B approaches B_{crit} . All modes apparently go to zero at or near B_{crit} . This behavior of $\omega^2(B)$ is consistent with the nonexistence of an equilibrium free surface nearby the critical one for $h_v \geqslant h_v^*$ and $B < B_{crit} < 0$. It is in sharp contrast to the behavior seen in

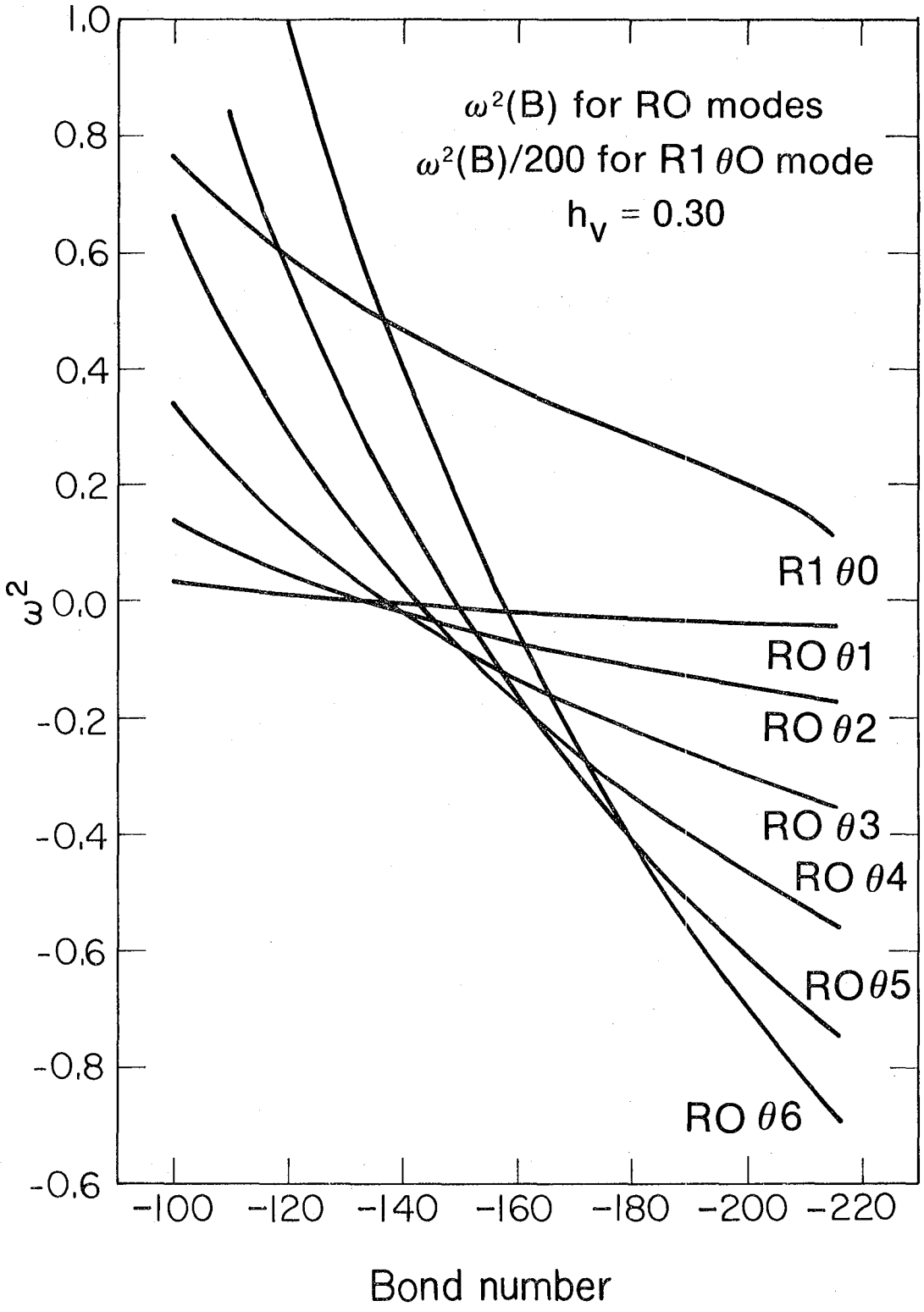

Figure 8. ω^2(B) of various modes for h_v = 0.30 . XBL781-96

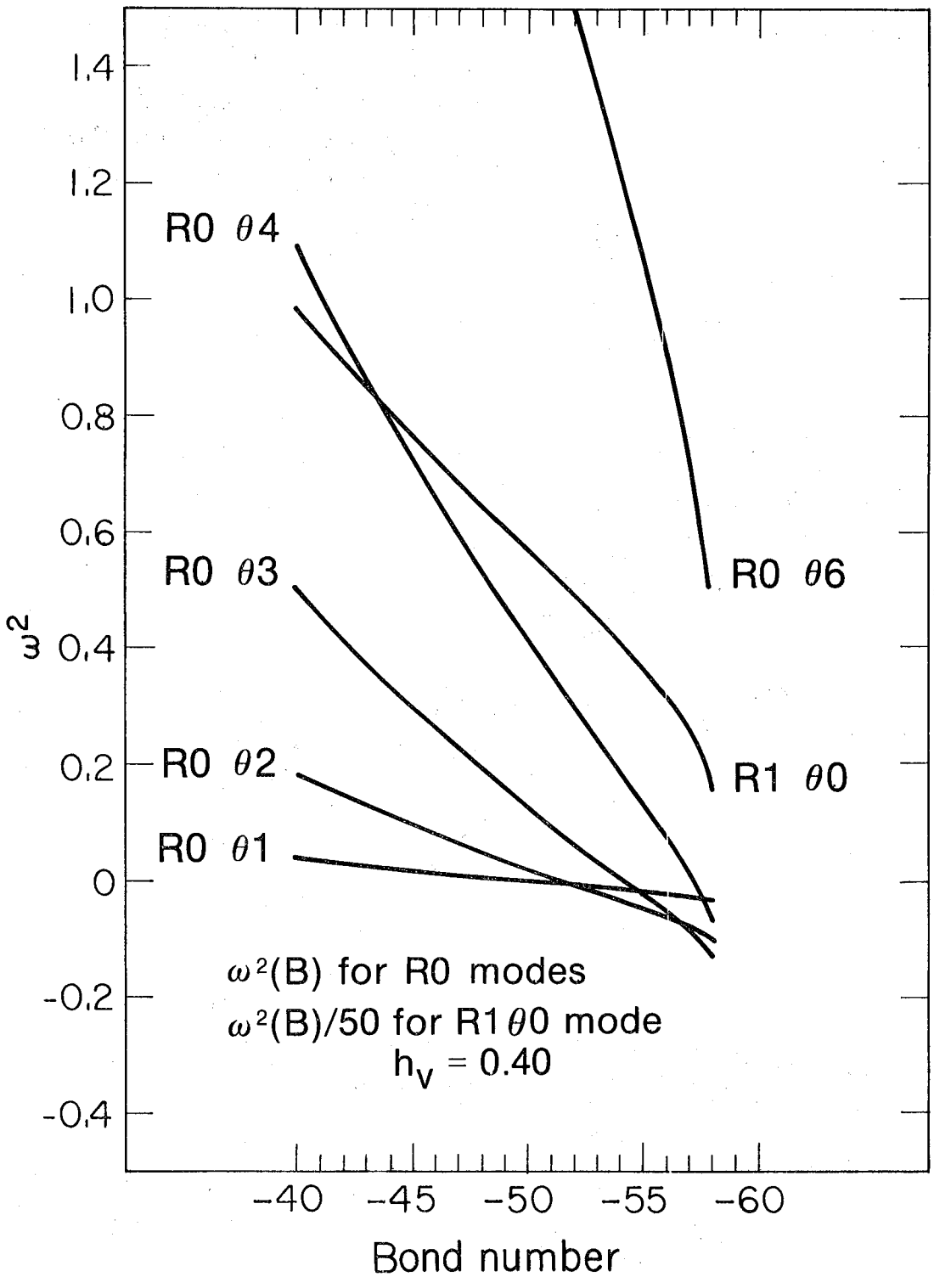

Figure 9. $\omega^2(B)$ of various modes for $h_v = 0.40$. XBL781-100

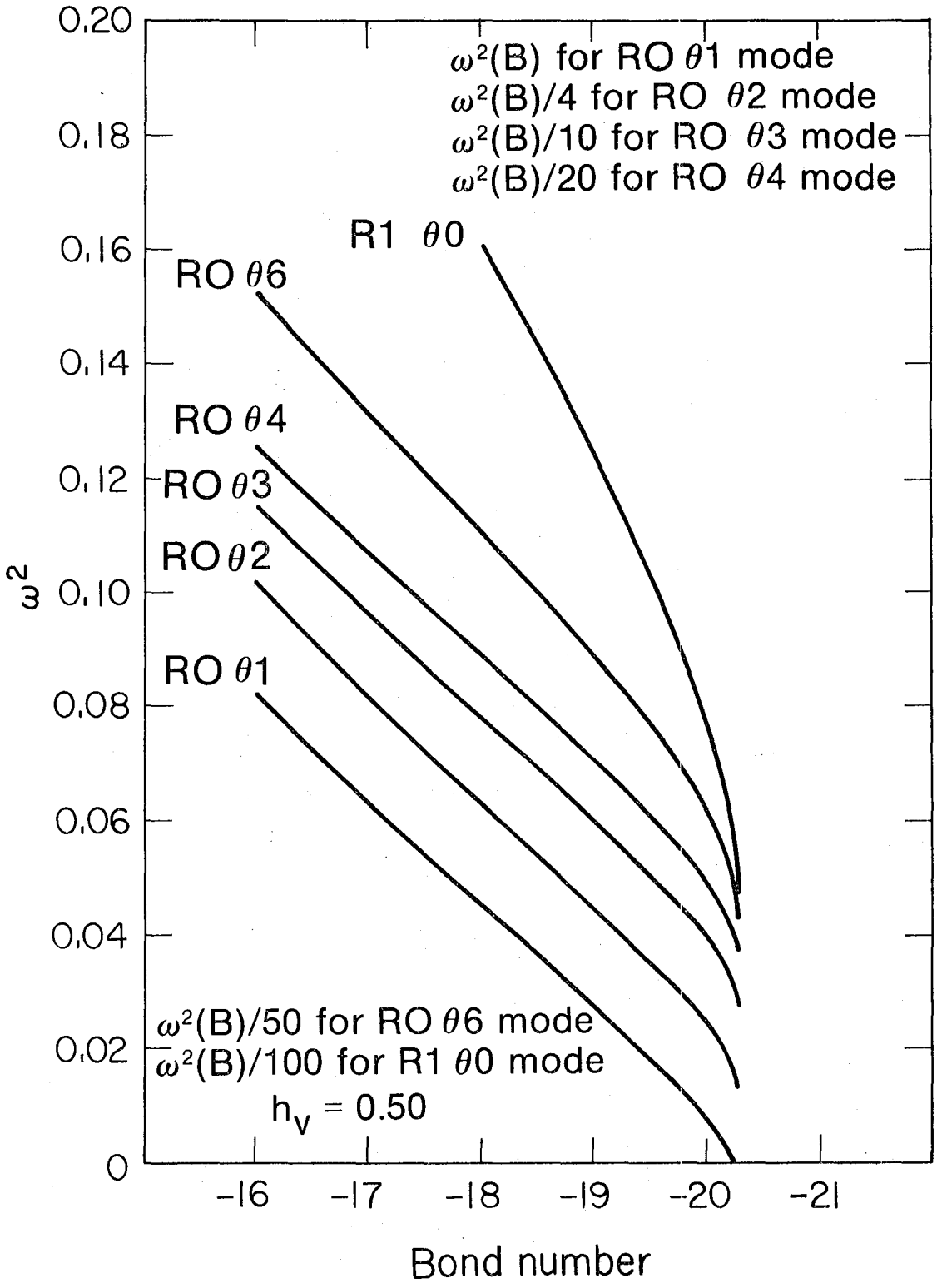

Figure 10. ω^2(B) of various modes for h_V = 0.50 . XBL 781-98

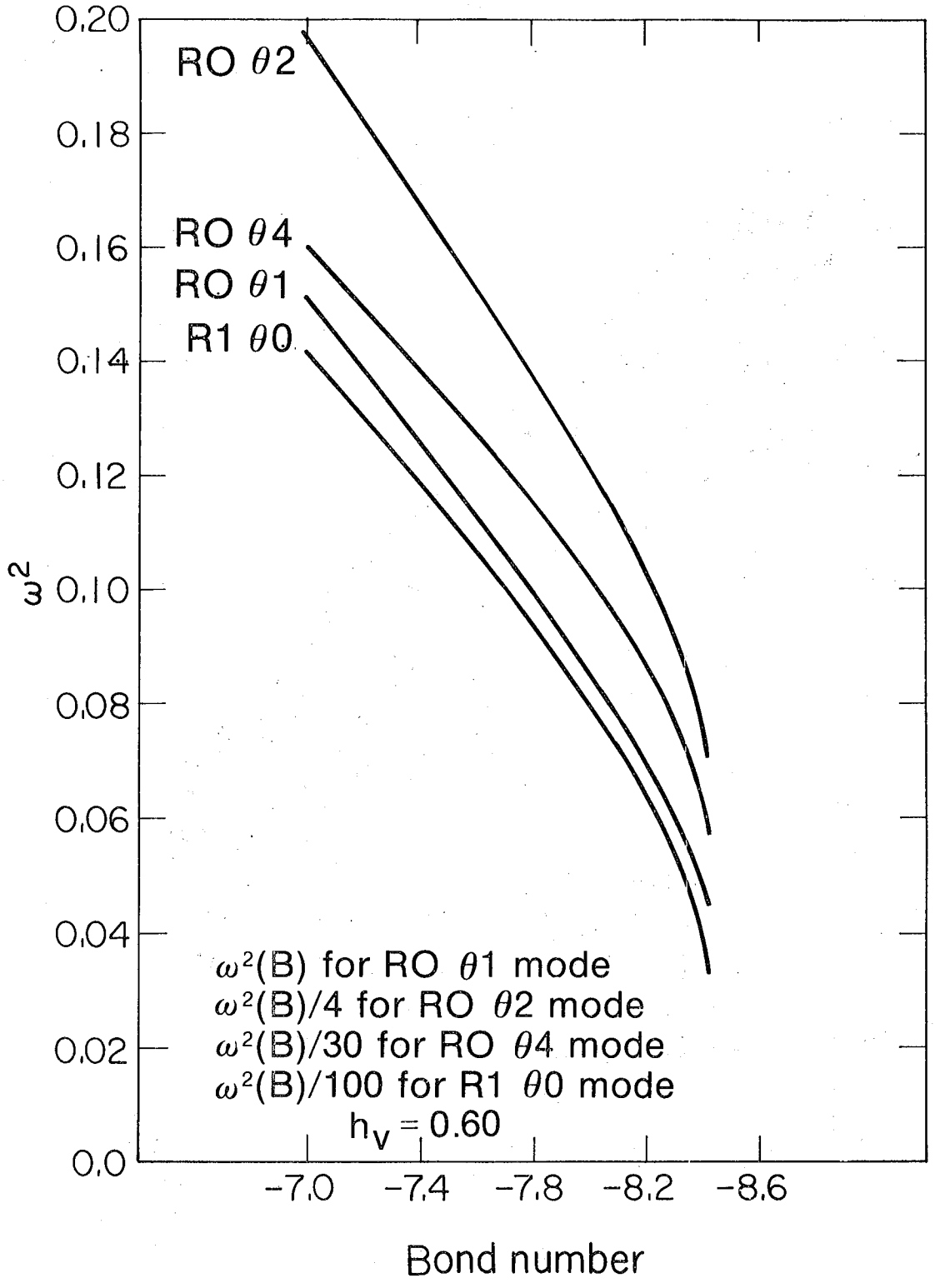

Figure 11. $\omega^2(B)$ of various modes for $h_v = 0.60$. XBL781-97

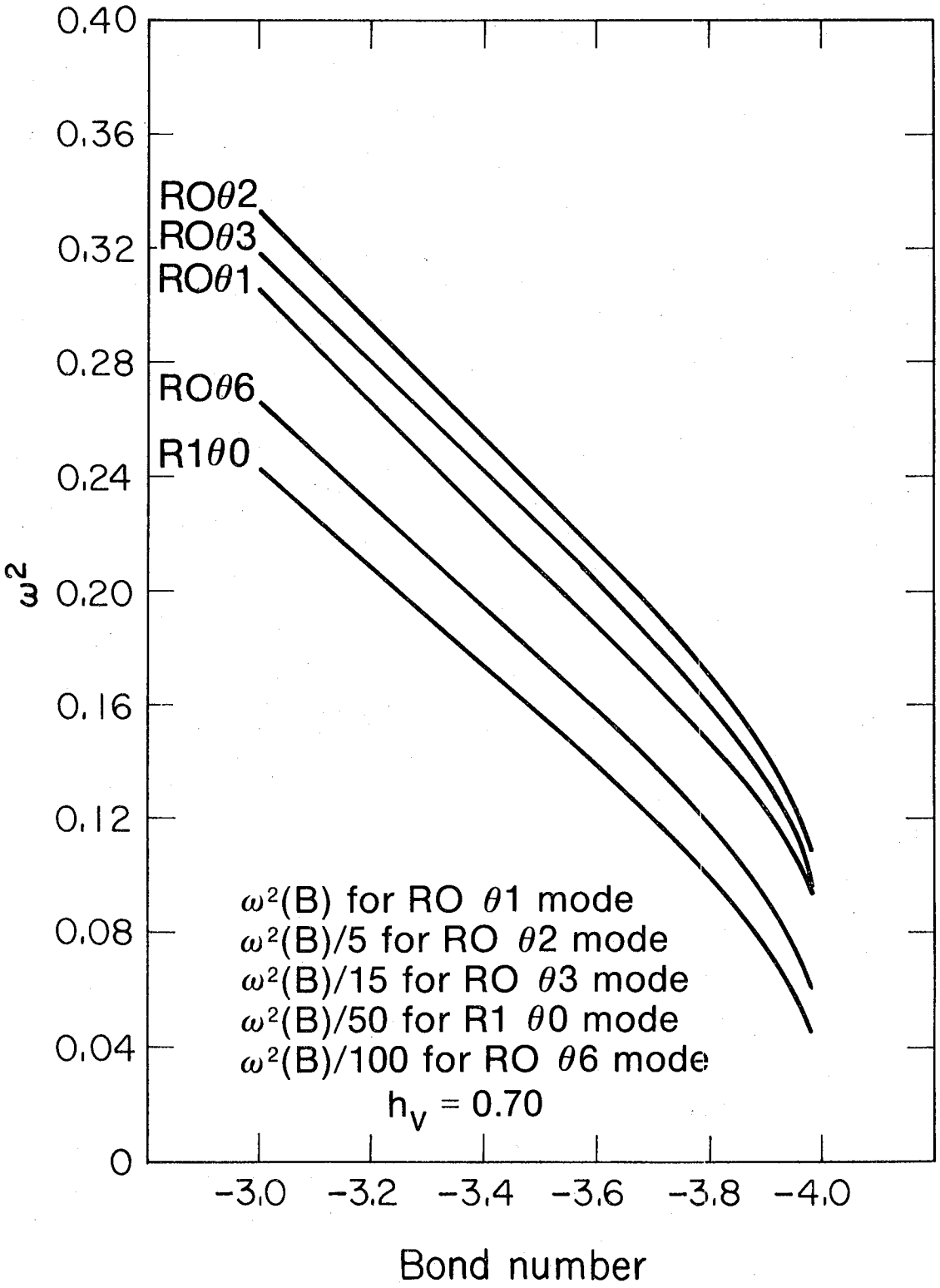

Figure 12. $\omega^2(B)$ of various modes for $h_v = 0.70$. XBL 781-99

the cases $h_v = 0.20\text{-}0.40$, in which only a few RO modes were unstable for a range of Bond numbers beyond B_{crit} .

For the case $h_v = 0.50$ the RO01 mode becomes marginally stable at a slightly higher Bond number than the other modes. In the 10-point approximation it becomes marginally stable at $B = -20.243$, while all the other modes approach instability as B approaches -20.276 . It appears that for this case there exists a very small range of Bond numbers between B_{crit} and B_{eq} .

12. Frequencies of the Normal Modes Continued -- Accuracy

The bulk of our data are values of ω^2 calculated by the 10-point approximation, Tables A 1 - A 11. Throughout this section we shall investigate the accuracy of these data. The few values of ω^2 calculated by the 20-point approximation are used solely to estimate the accuracy of these data and how they can be improved. We shall refer to these values as ω^2_{10} and ω^2_{20}, respectively.

We are most interested in the accuracy of ω^2_{10} for the growing RO modes. These negative values of ω^2 are small numbers, so a small (absolute) error in them can be significant. We shall show that the error in $\omega^2_{10}(B)$ is approximately $-(d\omega^2/dB)\Delta B^*$, where ΔB^* is a function of h_v but not of the mode number, that is,

$$\omega^2(B) \approx \omega^2_{10}(B) + (d\omega^2/dB)\Delta B^* , \tag{12.1}$$

or, equivalently,

$$\omega^2(B-\Delta B^*) \approx \omega^2_{10}(B) . \tag{12.2}$$

Thus, a value of $\omega^2_{10}(B)$ from Tables A 1, A 2, or A 4 actually corresponds to the Bond number $B-\Delta B^*$.

Five comparisons of calculated quantities support this description of the approximate dependence of the error in ω^2_{10} on the parameters h_v, B, and mode number. The first comparison is between the values of B_{crit} calculated by the 10-point approximation, which we shall denote by $B_{crit,10}$, and those calculated to four decimal places from a static analysis [1]. ΔB^* is defined as the difference in these values.

$$\Delta B^* = B_{crit,10} - B_{crit} .$$

These quantities are shown in Table 7. ΔB^* is approximately 1 - 2% of B_{crit}.

Table 7. B_{crit}, $B_{crit,10}$, and ΔB^* for three fill heights

h_v	$-B_{crit}$	$-B_{crit,10}$	ΔB^*
0.20	480.43	468.2	12.2
0.30	132.96	130.73	2.23
0.40	49.91	49.35	0.56

The second comparison is between the values of $\omega^2(B_{crit})$ for the ROθ1 mode calculated by the 10-point and 20-point approximations. Since the correct value of ω^2 is zero in this case, these values are errors. They show that the error in the calculated values of ω^2 depends as $1/N^2$ on the number of points used to approximate ϕ. These values are shown in Table 8. Note that ω_{20}^2 is approximately 1/4 of ω_{10}^2.

Table 8. ω_{10}^2 and ω_{20}^2 at B_{crit} for the ROθ1 mode.

h_v	$-\omega_{10}^2$	$-\omega_{20}^2$
0.20	0.00180	0.00045
0.30	0.00183	0.00046
0.40	0.00209	0.00053

The third comparison is between ω_{10}^2 and ω_{20}^2 for various RO modes, fill heights, and Bond numbers. Define $\Delta\omega^2$ as

$$\Delta\omega^2 = \omega_{20}^2 - \omega_{10}^2 \quad .$$

Since the error in ω_{20}^2 is approximately 1/4 of the error in ω_{10}^2, it follows that $\Delta\omega^2$ is approximately -3/4 of the error in ω_{10}^2. The values of $\Delta\omega^2$ are shown in Table 9. They vary greatly with mode number.

Table 9. $\Delta\omega^2$ for various RO modes, fill heights, and Bond numbers.

h_v	-B	ROθ1	ROθ2	ROθ3
0.30	130.	0.00141	0.0055	0.0120
	132.96	0.00137		
	140.	0.00127	0.0050	0.0108
0.40	45.	0.00193	0.0070	
	49.91	0.00156		
	50.		0.0059	

Define ΔB as

$$\Delta B = \Delta\omega^2 (dB/d\omega^2) \quad .$$

The values of $d\omega^2/dB$ can be calculated approximately by central differences of the data in Tables A 2 and A 4. The resulting values of ΔB are shown in Table 10. Note that for a given fill height, while $\Delta\omega^2$ varies greatly with mode number, ΔB does not. Our fourth comparison is between the values of ΔB and ΔB^*. Table 10 shows that the values of ΔB are approximately 3/4 of the corresponding values

of ΔB^* . Since $\Delta\omega^2$ is approximately -3/4 of the error in ω_{10}^2 , this implies that the error in ω_{10}^2 is approximately $-(d\omega^2/dB)\Delta B^*$ for some range of Bond numbers containing B_{crit} .

Table 10. ΔB for various RO modes, fill heights, and Bond numbers.

h_v	-B	ROθ1	ROθ2	ROθ3
0.30	130.	1.68	1.65	1.59
	132.96	1.71		
	140.	1.74	1.71	1.66
0.40	45.	0.47	0.43	
	49.91	0.44		
	50.		0.42	

For a given fill heights, let $B_{\theta n}$ denote the Bond number for which the ROθn mode becomes neutrally stable, that is, for which $\omega^2(B_{\theta n}) = 0$. Table 11 shows the values of the Bond numbers for the neutral stability of various modes as calculated by the 10-point approximation to ϕ , which we shall denote by $B_{\theta n,10}$. As B increases the various modes become unstable in order of increasing θ mode number, so $B_{\theta 1}$ is B_{crit} . We have already compared the accurate values of B_{crit} with the corresponding values of $B_{crit,10}$, that is, with $B_{\theta 1,10}$.

Table 11. $-B_{\theta n,10}$ for various modes and fill heights.

h_v	ROθ1	ROθ2	ROθ3	ROθ4	ROθ5	ROθ6
0.20	468.25	471.42	475.42	480.89		495.85
0.30	130.73	133.22	137.11	142.49	149.28	157.60
0.40	49.35	51.28	54.19	57.19		

Our last comparison is between the values of $B_{\theta n,10}$ and $B_{\theta n,20}$. Define $\Delta B_{\theta n}$ as

$$\Delta B_{\theta n} = B_{\theta n,10} - B_{\theta n,20} .$$

Table 12 shows values of $\Delta B_{\theta n}$ for various modes and fill heights. It shows that the values of $\Delta B_{\theta n}$ are approximately 3/4 of the corresponding values of ΔB^*. For a given fill height $\Delta B_{\theta n}$ is approximately the same for each mode. This implies that the error in ω_{10}^2 is approximately $-(d\omega^2/dB)\Delta B^*$ for some range of Bond numbers containing these $B_{\theta n}$.

Table 12. $\Delta B_{\theta n}$ for various modes and fill heights.

h_v	ROθ1	ROθ2	ROθ3
0.30	1.68	1.69	1.59
0.40	0.42	0.42	

When the values of $B_{\theta n}$ given in Table 11 are adjusted by adding ΔB^*, the values shown in Table 13 are obtained.

Table 13: Adjusted values of $-B_{\theta n}$ for various modes and fill heights.

h_v	ROθ1	ROθ2	ROθ3	ROθ4	ROθ5	ROθ6
0.20	480.43	483.6	487.6	493.1		508.0
0.30	132.96	135.5	139.3	144.7	151.5	159.8
0.40	49.91	51.8	54.8	57.8		

We consider finally the R1 modes. Table 14 shows the relative difference in ω^2 calculated with the 10-point and 20-point approximations, that is, $(\omega_{20}^2 - \omega_{10}^2)/\omega_{10}^2$. The value of ω^2 differed by 10% for the R1θ1 mode with $h_v = 0.20$. It differed by 2.6 - 2.7% for the R1θ1 and R1θ2 modes with $h_v = 0.40$ for Bond number 55, which is near B_{div}. The value of ω^2 differed by only 1 - 2% for all the R1 modes with $h_v = 0.30$ or 0.40 and Bond numbers not near B_{div}.

Table 14. Range of $\Delta\omega^2/\omega^2$ for various modes and fill heights.

h_v	range of -B	R1θ1	R1θ2	R1θ3
0.20	450.-500.	0.100		
0.30	130.-140.	0.015-0.016	0.015-0.016	0.015-0.016
0.40	45.- 50.	0.015-0.019	0.014-0.019	
0.40	55.	0.026	0.027	

13. Growth Rates and Accuracy for Fill Height = 0.30

Figure 8 and Table A 2 show $\omega^2(B)$ of the various RO modes for $h_v = 0.30$. They show which is the maximally unstable mode for each value of B . The information for the maximally unstable mode is displayed in Table 15. The values of B listed in this table have been adjusted by ΔB^* .

For example, the ROθ1 mode is the maximally unstable one for $-134.04 < B < -132.96$, the ROθ2 mode for $-140.27 < B < -134.04$, etc. The value of $(d\omega^2/dB)\Delta B^*$ is an estimate of the accuracy of ω^2 before adjustment by ΔB^* . We feel the error remaining in ω^2 after this adjustment is less than $(d\omega^2/dB)\Delta B^*$. In particular, we feel the errors remaining in ω^2 for the ROθ1 , ROθ2 , and ROθ3 modes are 1/10 to 1/4 of $(d\omega^2/dB)\Delta B^*$.

Table 15. $\omega^2(B)$ of the maximally unstable mode for $h_v = 0.30$.

-B	ω^2	maximally unstable	$(d\omega^2/dB)\Delta B^*$
132.96	0.0		
		ROθ1	0.0017
134.04	0.0025		
		ROθ2	0.007
140.27	0.0218		
		ROθ3	0.014
149.99	0.0808		
		ROθ4	0.021
163.48	0.204		
		ROθ5	0.028
179.76	0.407		
		ROθ6	0.032
202.23	0.701		

The dimensionless growth rate Γ of the maximally unstable mode is shown in Table 16. The corresponding growth period in seconds is

$$\Gamma^{-1}(\bar{t}/t) = \Gamma^{-1}[\rho a^3/\sigma(1+|B|)]^{\frac{1}{2}} \quad .$$

This is calculated for a cylinder of radius 7 cm for the three liquids ethanol, freon, and FC78. The values of ρ/σ used for these were 0.03538, 0.08489, and 0.131 sec^2/cm^3, respectively. Ethanol has the fastest growth rates and FC78 has the slowest. B_{crit} is -132.96 for this case. At Bond number $B = -150$ the growth periods range from 1.0 to 1.9 sec. At $B = -202$, which is 50% beyond B_{crit}, they range from 0.29 to 0.56 sec. It is not likely that growth would be observed in these cases in an experiment with a negative-B phase of only 2.5 sec, since only 2-8 growth periods would elapse.

Table 16. Maximal growth rates and growth periods for $h_v = 0.30$.

dimensionless values		growth period (sec)		
-B	Γ	ethanol	freon	FC78
132.96	0.0	∞	∞	∞
134.04	0.050	5.9	9.2	11.4
140.27	0.148	1.99	3.1	3.8
149.99	0.284	1.00	1.54	1.92
163.48	0.451	0.60	0.93	1.16
179.76	0.638	0.41	0.63	0.78
202.23	0.837	0.29	0.45	0.56

The errors in ω^2 for the smaller values of ω^2 (the ROθ1, ROθ2, and ROθ3 modes) have a greater percentage reduction from the ΔB^* adjustment than those for larger values of ω^2. However, these

errors were initially larger fractions of their values of ω^2 than those for the larger values of ω^2 . As a result of these two effects, the errors in ω^2 remaining after this adjustment probably lie in the range 5 - 20%, the larger values of ω^2 being more accurate. The corresponding errors in the growth rate probably lie in the range 2 - 10% . However, these are only the computational errors in Γ ; they represent the accuracy with which the growth rates were calculated from the assumed model of the liquid motion. The accuracy with which they describe experimentally observed growth rates depends also on the accuracy of that model. In this model the fluid motion was assumed to be nonviscous and irrotational, and the contact angle was assumed to be time independent. These assumptions could be tested by computing the fluid motion with a complete hydrodynamics code that includes all the relevant effects.

14. Summary

In this paper we calculate the small-amplitude periodic sloshing modes of a liquid in a vertical right circular cylinder with a concave spheroidal bottom, for the case in which there is not sufficient liquid to cover the bottom entirely. Numerical results are obtained for a container currently used for the storage of liquid fuels in the Centaur space vehicles, for which the axial ratio of the bottom is $b/a = 0.724$.

We follow the derivation in [2] for obtaining the equations of motion for the case studied here, but we use a different technique for obtaining the numerical solution. The liquid is subject to surface and gravitational forces. The equilibrium surface is the solution of the time-independent Bernoulli equation subject to a contact-angle condition.

It is assumed for the dynamical equations that the fluid flow is irrotational and incompressible. The fluid velocity is the gradient of a potential function that satisfies Laplace's equation. The velocity potential and its gradient on the free surface are related by the linearized time-dependent Bernoulli equation and the contact-angle condition. The sloshing motion is analyzed in terms of normal modes. The discrete form of these equations yields a generalized eigenvalue problem for ω^2 , the square of the normal-mode frequency. This problem was solved numerically using the IMSL routine EIGZF.

The accuracy of this numerical procedure was tested by calculating the eigenvalues and eigenvectors for the small-amplitude periodic sloshing modes of a liquid contained between two concentric vertical

circular cylinders for contact angle $\gamma = 90°$ and comparing with the known analytic solution for this case. The numerical values of ω^2 were correct typically to about 1 or 2%, a satisfactory accuracy for our purposes.

Equilibrium surfaces of a liquid in a vertical circular cylinder with a concave spheroidal bottom were calculated for contact angle $\gamma = 0°$, axial ratio of the spheroidal bottom $b/a = 0.724$, fill heights h_v ranging from 0.20 to 0.70, and many values of the Bond number. These equilibrium surfaces are members of a family with parameters B and h_v. B_{crit} was defined above as the critical value of the Bond number for the stability of surfaces of this family for a given fill height. B_{eq} was defined as the critical value of the Bond number for the nonexistence of equilibrium surfaces of this family. Stable equilibrium surfaces exist for $B_{crit} \leqslant B$, unstable equilibrium surfaces exist for $B_{eq} \leqslant B < B_{crit} < 0$ if $B_{eq} \neq B_{crit}$, and no equilibrium surfaces exist for $B < B_{eq}$.

For all the values of the fill height that were studied, stable equilibrium surfaces were found for a range of Bond numbers, $B_{crit} \leqslant B \leqslant 0$. To the accuracy of these calculations, we found the same value for B_{crit} as was found in the static analysis of the same problem [1].

For fill heights ranging from 0.20 to 0.45, we found unstable equilibrium surfaces for a range of Bond numbers $B_{conv} \leqslant B < B_{crit}$, but no equilibrium surfaces of this family were found for $B \leqslant B_{div} < B_{conv}$. ($B_{conv}$ and B_{div} are approximations to B_{eq}.)

For $h_v = 0.50$ unstable equilibrium surfaces were found for a very small range of Bond numbers. For $h_v = 0.60$ and 0.70 no equilibrium surfaces of this family were found for $B < B_{crit}$. To the accuracy of these calculations, these results are consistent with [1], which found that $B_{eq} = B_{crit}$ for $h_v \geq h_v^* = 0.503$, but that $B_{eq} < B_{crit}$ for $h_v < h_v^*$.

The qualitative nature of the stability of the individual normal modes differs for the two cases $h_v < h_v^*$ and $h_v \geq h_v^*$. For fill heights $h_v = 0.20$, 0.30, and 0.40, the normal modes $RO\theta1$, $RO\theta2$, $RO\theta3$, ... become marginally stable at a sequence of Bond numbers $\ldots B_{\theta3} < B_{\theta2} < B_{\theta1} = B_{crit} < 0$. Each RO mode is the fastest growing mode for a small range of Bond numbers. For fill heights $h_v = 0.60$ and 0.70 all the modes that were studied approach instability as the Bond number approaches B_{crit}. For each mode the function $\omega^2(B)$ curves toward the $\omega^2 = 0$ axis, approaching zero with increasing rapidity as B approaches B_{crit}. For $h_v = 0.50$, which is near the critical fill height h_v^*, the $RO\theta1$ mode becomes marginally stable at a slightly higher Bond number than the other modes. The instability of all modes for $h_v \geq h_v^*$ and $B < B_{crit}$ is consistent with the nonexistence of equilibrium surfaces nearby the critical one for this range of parameters.

Most of the calculations of ω^2 were made by approximating the velocity potential on a meridian along the free surface by its value at 10 points. It was possible to correct partially these calculated values of ω^2 by applying an adjustment based on a study of the errors.

Growth rates of the maximally unstable mode were calculated for the case $h_v = 0.30$ using the adjusted values of ω^2. Each of the modes ROθ1, ROθ2, ... ROθ6, in succession, was the maximally unstable one for a small range of Bond numbers. The corresponding growth periods in seconds were calculated for a cylinder of radius 7 cm for the three liquids ethanol, freon, and FC78. Ethanol has the fastest growth rates and FC78 has the slowest. B_{crit} is -132.96 for this case. At Bond number $B = -150$ the growth periods range from 1.0 to 1.9 sec. At $B = -202$, which is 50% beyond B_{crit}, they range from 0.29 to 0.56 sec. It is not likely that growth would be observed in these cases in an experiment with a negative-B phase of only 2.5 sec, since only 2 to 8 growth periods would elapse.

ACKNOWLEDGMENTS

We would like to thank Eugene P. Symons for stimulating our interest in this problem and for sharing experimental data related to it. We would also like to thank Said Doss for developing and programming the Laplace solver that was used in the program SLOSH and Ru-Mei Kung for adapting the program CAPIL for use on the LBL computer system.

This work was supported in part by the National Aeronautics and Space Administration and by the Department of Energy.

REFERENCES

1. P. Concus and I. Karasalo, "A Numerical Study of Capillary Stability in a Circular Cylindrical Container with a Concave Spheroidal Bottom," Lawrence Berkeley Laboratory Report LBL-6144, (1977).

2. P. Concus, G.E. Crane, H.M. Satterlee, "Small Amplitude Lateral Sloshing in Spheroidal Containers under Low Gravitational Conditions," NASA CR-72500 Lewis Research Center, Cleveland, Ohio (1969).

3. P. Concus and V. Pereyra, "CAPIL: A Package for Meniscus Computations," Lawrence Berkeley Laboratory Report (to be published).

4. M. Lentini and V. Pereyra, "An Adaptive Finite Difference Solver for Nonlinear Two-point Boundary Problems with Mild Boundary Layers," SIAM J. Numer. Anal. 14, 91 (1977).

5. S. Doss, "Numerical Solution of the Rotationally Separable Laplace Equation by an Integral Equation Method," Lawrence Berkeley Laboratory Report (to be published).

6. E.P. Symons (private communication).

LIST OF SYMBOLS

a	Radius of cylindrical container and horizontal semiaxis of spheroidal bottom.
A	Diagonal matrix in the discretized time-dependent Bernoulli equation.
b	Vertical semiaxis of spheroidal bottom.
B	Bond number $= \kappa a^2$.
B_{crit}	Critical Bond number for stability of equilibrium surfaces.
B_{eq}	Critical Bond number for the nonexistence of equilibrium surfaces of the family considered in this report.
B_{conv}, B_{div}	Approximations to B_{eq} .
$B_{\theta m}$	Critical Bond number for stability of the $R0\theta m$ mode.
c,d	Constants in a linear combination of Bessel functions.
C	Matrix in the discrete solution of the Laplace equation.

D, E, F	Matrices.
$\mathcal{D}$	A rectangular domain.
e_j	Vector with a one in the j^{th} position and zeros elsewhere.
g	Acceleration due to gravity, considered positive when directed vertically downward.
h_v	Dimensionless fill height.
h_v^*	Critical h_v for existence of unstable equilibrium surfaces of the family considered in this report. These exist for $h_v < h_v^*$ and $B_{eq} \leqslant B < B_{crit}$.
$\bar{H}$	Mean curvature at a point on the free surface, considered negative when the surface is concave upward.
H	Scaled mean curvature = $\bar{H}a$.
H_0	A constant = $(p_g - p_0)a/2\sigma$, interpreted as the extrapolated value of H at the height $z = 0$.
$\tilde{H}(s,\theta,t)$	Displacement η of the free surface.
$H(s)$	A factor in the normal mode expression of the displacement of the free surface.
J_m	Bessel function of the first kind of order m .

k	The argument of the Bessel function is kr .
K, L	Terms representing the contact-angle conditions.
m	Number of angular nodes in the normal mode.
M	The meridians of the cylinder wall and spheroidal bottom in the cross-sectional plane are divided into M intervals.
n	Each of the meridians of the free surface, cylinder walls, and flat bottom in the cross-sectional plane of two concentric cylinders is divided into n intervals.
subscript n	Outward normal derivative.
N	The meridian of the free surface in the cross-sectional plane is divided into N intervals.
p_g	Gas pressure.
p_0	Liquid static pressure at the height $z = 0$.
P_j	The integral of $Q(s)\ R(s)$ over the j^{th} interval.
Q(s), Q(r)	A functional of the free surface appearing in the linearized Bernoulli equation.
$\bar{r}$	Radial coordinate.
r	Scaled radial coordinate = $\bar{r}/a$.
subscript r	d/dr .

r_0, r_1	Radii of two concentric right circular cylinders.
R(s)	Radius of the equilibrium free surface as a function of the arc length along the meridian.
RO, R1, R2, ...	Normal modes with 0, 1, 2, ... radial nodes in ϕ .
s	Arc length along the meridians of the free surface, cylinder wall, and spheroidal bottom in the cross-sectional plane: $0 \leqslant s \leqslant S$ on the free surface.
subscript s	d/ds .
s, θ, η	Surface polar normal coordinates.
s_1, s_2, ... s_N	Midpoints of the N intervals on the meridian of the free surface in the cross-sectional plane.
$\bar{t}$	Time coordinate.
t	Scaled time coordinate = $\bar{t}[(1+\|B\|)\sigma/\rho a^3]^{\frac{1}{2}}$
subscript t	d/dt .
t_1, t_2, ... t_{N+1}	Endpoints of the N intervals on the meridian of the free surface in the cross-sectional plane.
T	Tridiagonal matrix in the discretized time-dependent Bernoulli equation.

$U(z)$	A factor of the velocity potential in the liquid contained between two concentric cylinders.
v	Fluid velocity.
V	Volume of the liquid in the cylinder.
W	Matrix in the discrete solution of the Laplace equation.
$X(r)$	A factor of the velocity potential in the liquid contained between two concentric cylinders.
Y_m	Bessel function of the second kind of order m .
$\bar{z}$	Vertical coordinate.
z	Scaled vertical coordinate = $\bar{z}/a$.
z_0	Height of liquid contained between two concentric cylinders.
$Z(s)$	Height of the equilibrium surface as a function of the radius.
$Z_B(r)$	Height of the spheroidal bottom as a function of the radius.
γ	Contact angle.
Γ	Dimensionless growth rate of maximally growing mode.
ΔB	$= \Delta\omega^2/(d\omega^2/dB)$.

ΔB^*	$= B_{crit,10} - B_{crit}$, where $B_{crit,10}$ is the value of B_{crit} calculated by the 10-point approximation.
$\Delta B_{\theta n}$	$= B_{\theta n,10} - B_{\theta n,20}$.
$\Delta\omega^2$	$= \omega_{20}^2 - \omega_{10}^2$, where ω_{20}^2 and ω_{10}^2 are the values of ω^2 calculated by the 20- and 10-point approximations, respectively.
η	Displacement normal to the equilibrium surface.
θ	Angle around the cylinder axis.
$\theta 0$, $\theta 1$, $\theta 2$, ...	Normal modes with 0, 1, 2, ... angular nodes.
κ	Capillary constant = $\rho g/\sigma$.
ρ	Difference in densities between the liquid and gas phases.
σ	Gas-liquid surface tension.
$\tilde{\phi}(r,z,\theta,t)$	Potential function for the fluid velocity.
$\phi(r,z)$	A factor in the normal mode expression of velocity potential.
Φ_1	Vector of values of ϕ at N points on the meridian on the free surface.

Φ_2 Vector of values of ϕ at M points on the meridians on the cylinder wall and bottom.

Φ Vector = (Φ_1, Φ_2) .

χ Angle in the cross-sectional plane between the horizontal and the tangent to the meridian on the bottom.

ψ Angle in the cross-sectional plane between the horizontal and the tangent to the meridian on the free surface.

ω Frequency of the normal mode.

Table A 1. $\omega^2(B)$ for various θ modes; fill height = 0.20; radial mode = RO.

-Bond	θ1	θ2	θ3	θ4	θ6
200.	0.0910	0.363	0.817	1.46	3.30
400.	0.0116	0.0473	0.111	0.208	0.535
450.	0.0027	0.0121	0.032	0.069	0.226
500.	-0.0044	-0.0161	-0.031	-0.043	-0.020
550.	-0.0101	-0.0392	-0.083	-0.134	-0.223
600.	-0.0151	-0.0585	-0.126	-0.210	-0.392
700.	-0.0227	-0.0889	-0.194	-0.330	-0.657
800.	-0.0285	-0.112	-0.245	-0.420	-0.856
900.	-0.0330	-0.130	-0.285	-0.491	-1.01
1000.	-0.0366	-0.144	-0.317	-0.547	-1.14

Table A 2. $\omega^2(B)$ for various θ modes; fill height = 0.30; radial mode = RO.

-Bond	θ1	θ2	θ3	θ4	θ5	θ6
50.	0.170	0.686	1.57	2.86	4.60	6.84
100.	0.0328	0.139	0.339	0.666	1.16	1.86
110.	0.0202	0.0883	0.226	0.464	0.841	1.40
120.	0.0096	0.0460	0.131	0.295	0.576	1.01
130.	0.0006	0.0100	0.050	0.151	0.351	0.688
140.	-0.0072	-0.0210	-0.020	0.027	0.157	0.407
150.	-0.0140	-0.0481	-0.081	-0.081	-0.012	0.163
160.	-0.0200	-0.0720	-0.135	-0.176	-0.160	-0.051
180.	-0.0302	-0.113	-0.225	-0.336	-0.410	-0.411
200.	-0.0389	-0.147	-0.301	-0.468	-0.612	-0.701
210.	-0.0431	-0.163	-0.336	-0.527	-0.701	-0.826
216.	-0.0462	-0.175	-0.358	-0.562	-0.750	-0.892

Table A 3. $\omega^2(B)$ for various θ modes; fill height = 0.30; radial mode = R1.

-Bond	θ0	θ2	θ4	θ6
50.	350.	352.	359.	370.
100.	153.	154.	158.	163.
110.	135.	136.	139.	144.
120.	119.	120.	123.	127.
130.	105.	106.	109.	113.
140.	93.5	94.4	96.8	101.
150.	82.9	83.7	86.1	89.8
160.	73.3	74.1	76.3	79.8
180.	56.1	56.9	58.9	62.1
200.	39.6	40.3	42.2	45.1
210.	30.1	30.7	32.5	35.2
216.	21.1	21.7	23.4	25.8

Table A 4. $\omega^2(B)$ for various θ modes; fill height = 0.40; radial mode = RO.

-Bond	$\theta 1$	$\theta 2$	$\theta 3$	$\theta 4$	$\theta 6$
20.	0.225	0.936	2.24	4.28	11.3
40.	0.0384	0.182	0.503	1.10	3.52
45.	0.0161	0.0920	0.298	0.724	2.59
50.	-0.0024	0.0172	0.127	0.411	1.81
55.	-0.0193	-0.0498	-0.025	0.133	1.09
56.	-0.0229	-0.0635	-0.055	0.077	0.938
57.	-0.0268	-0.0784	-0.088	0.017	0.768
58.	-0.0329	-0.100	-0.134	-0.069	0.497

Table A 5. $\omega^2(B)$ for various θ modes; fill height = 0.40; radial mode = R1.

-Bond	θ0	θ2	θ4	θ6
20.	132.	135.	144.	158.
40.	49.2	50.8	55.4	62.8
45.	38.2	39.7	43.8	50.2
50.	28.3	29.6	33.2	38.9
55.	18.1	19.3	22.3	27.0
56.	15.8	16.8	19.7	24.2
57.	13.0	14.0	16.7	20.7
58.	8.07	8.89	11.1	14.3

Table A 6. $\omega^2(B)$ for various θ modes; fill height = 0.50; radial mode = RO.

-Bond	θ1	θ2	θ3	θ4	θ6
8.	0.359	1.56	3.93	7.88	22.1
16.	0.0821	0.407	1.15	2.51	7.62
18.	0.0455	0.254	0.782	1.78	5.53
19.	0.0281	0.181	0.604	1.42	4.46
20.	0.0082	0.0993	0.398	0.989	3.09
20.1	0.0055	0.0882	0.369	0.926	2.88
20.2	0.0021	0.0743	0.333	0.845	2.61
20.25	-0.0003	0.0645	0.306	0.785	2.40
20.2759	-0.0027	0.0549	0.280	0.722	2.18

Table A 7. $\omega^2(B)$ for various θ modes; fill height = 0.50; radial mode = R1.

-Bond	θ0	θ2	θ4	θ6
8.	71.1	75.8	89.6	113.
16.	23.3	25.8	32.7	44.6
18.	16.1	18.1	24.0	34.1
19.	12.4	14.2	19.4	28.4
20.	7.75	9.24	13.4	20.9
20.1	7.06	8.49	12.5	19.7
20.2	6.17	7.53	11.3	18.0
20.25	5.52	6.80	10.4	16.8
20.2759	4.85	6.06	9.41	15.5

Table A 8. $\omega^2(B)$ for various θ modes; fill height = 0.60; radial mode = RO.

-Bond	θ1	θ2	θ3	θ4	θ6
3.5	0.531	2.47	6.62	13.8	39.0
7.0	0.152	0.790	2.26	4.81	13.4
8.0	0.0849	0.487	1.44	3.06	8.16
8.2	0.0697	0.415	1.24	2.61	6.81
8.4	0.0483	0.308	0.917	1.88	4.59
8.41	0.0466	0.299	0.889	1.81	4.40
8.42	0.0443	0.286	0.847	1.72	4.11

Table A 9. $\omega^2(B)$ for various θ modes; fill height = 0.60; radial mode = R1.

-Bond	θ0	θ2	θ4	θ6
3.5	44.3	51.5	73.7	117.
7.0	14.2	17.8	28.9	51.3
8.0	7.98	10.7	19.0	35.8
8.2	6.39	8.82	16.2	31.0
8.4	3.83	5.70	11.3	22.4
8.41	3.61	5.43	10.8	21.6
8.42	3.30	5.04	10.2	20.6

Table A 10. $\omega^2(B)$ for various θ modes; fill height = 0.70; radial mode = RO.

-Bond	θ1	θ2	θ3	θ4	θ6
1.5	0.771	3.94	11.1	23.5	65.1
3.0	0.306	1.67	4.79	9.99	26.6
3.2	0.266	1.47	4.20	8.72	23.0
3.4	0.227	1.27	3.63	7.49	19.5
3.6	0.188	1.07	3.06	6.22	15.9
3.8	0.148	0.855	2.40	4.78	11.8
3.9	0.124	0.719	1.98	3.86	9.26
3.94	0.111	0.647	1.75	3.36	7.93
3.98	0.0945	0.543	1.42	2.65	6.07

Table A 11. $\omega^2(B)$ for various θ modes; fill height = 0.70; radial mode = R1.

-Bond	θ0	θ2	θ4	θ6
1.5	30.7	41.5	78.5	162.
3.0	12.2	18.1	38.6	85.7
3.2	10.4	15.8	34.5	77.6
3.4	8.67	13.6	30.5	69.2
3.6	6.91	11.2	26.2	59.8
3.8	4.96	8.59	21.1	48.3
3.9	3.75	6.89	17.7	40.7
3.94	3.14	6.02	15.9	36.6
3.98	2.30	4.79	13.3	30.9